Chemical Science

ROYAL SOCIETY OF CHEMISTRY

REVIEW

View Article Online
View Journal | View Issue

Cite this: *Chem. Sci.*, 2024, **15**, 5082

Structural engineering of atomic catalysts for electrocatalysis

Tianmi Tang, Xue Bai, Zhenlu Wang and Jingqi Guan *

As a burgeoning category of heterogeneous catalysts, atomic catalysts have been extensively researched in the field of electrocatalysis. To satisfy different electrocatalytic reactions, single-atom catalysts (SACs), diatomic catalysts (DACs) and triatomic catalysts (TACs) have been successfully designed and synthesized, in which microenvironment structure regulation is the core to achieve high-efficiency catalytic activity and selectivity. In this review, the effect of the geometric and electronic structure of metal active centers on catalytic performance is systematically introduced, including substrates, central metal atoms, and the coordination environment. Then theoretical understanding of atomic catalysts for electrocatalysis is innovatively discussed, including synergistic effects, defect coupled spin state change and crystal field distortion spin state change. In addition, we propose the challenges to optimize atomic catalysts for electrocatalysis applications, including controlled synthesis, increasing the density of active sites, enhancing intrinsic activity, and improving the stability. Moreover, the structure–function relationships of atomic catalysts in the CO_2 reduction reaction, nitrogen reduction reaction, oxygen reduction reaction, hydrogen evolution reaction, and oxygen evolution reaction are highlighted. To facilitate the development of high-performance atomic catalysts, several technical challenges and research orientations are put forward.

Received 24th January 2024
Accepted 5th March 2024

DOI: 10.1039/d4sc00569d

rsc.li/chemical-science

1. Introduction

More than 80% of modern chemical industrial processes involve catalytic reactions, which have greatly promoted the development of modern industry.[1] Therein, the wide application of electrocatalysis technology reduces the industrial dependence on fossil fuels and alleviates the environmental crisis, for instance, CO_2 can be converted into chemicals with high added value through the electrocatalytic CO_2 reduction reaction (CO_2RR).[2,3] Fuel cells and water splitting are new energy conversion technologies, in which no carbon-containing compounds are released and the core reactions are the oxygen reduction reaction (ORR), oxygen evolution reaction (OER) and hydrogen evolution reaction (HER).[4–7] Ammonia synthesis by the Haber–Bosch process requires high temperature and high pressure, which can be achieved by the electrocatalytic nitrogen reduction reaction (NRR) at normal temperature and normal pressure. Moreover, the electrocatalytic NRR can be used to treat wastewater and reduce nitrogen pollution.[8] However, the application of electrocatalysis to industry not only requires high catalytic activity and specific selectivity, but also needs to ensure economic benefit and high catalytic stability. The commonly used electrocatalysts are Pt, Au, Ru, Ir and other precious metals, but their small reserves and high price hinder the large-scale commercial applications.[3,9] The development of efficient and economical transition metal-based catalysts is expected to promote the development of industrial electrocatalysis.

By reducing the size of metal particles of metal-based catalysts from bulk to nanoscale, and further to the single-atom level, atomic dispersion of metal species is achieved. In 1998, Basset *et al.* modified Sn atoms around Pt atoms by surface organometallic chemistry (SOMC), showing nearly 100% selectivity for isobutane dehydrogenation.[10] In addition, they used the Si–O bond on the surface of silicon oxide to fix single Zr atoms, which can be used for low-temperature hydrogenolysis of alkanes.[11] In 2011, the concept of "single atom catalysis" was first proposed by Zhang *et al.*[12] Single-atom catalysts (SACs) are a new catalytic family. The uniformly dispersed isolated metal atoms on the substrate have well-defined active centers and 100% atom utilization.[13]

As a new family of catalysts, isolated transition metal atoms in SACs anchored to specific substrates act as active sites. In addition to the central metal, the surrounding coordination environment affects the electronic structure and geometric configuration of single metal sites, and the catalytic activity of SACs is related to the strong force between metal centers and the substrate. Therefore, the electrocatalytic activity can be effectively improved by selecting appropriate central metal atoms and adjusting the local microenvironment of SACs.[14,15] Diatomic catalysts (DACs) have isolated pairs of metal atoms as the active sites, in which pairs of the same metal are called

Institute of Physical Chemistry, College of Chemistry, Jilin University, Changchun 130021, PR China. E-mail: guanjq@jlu.edu.cn

homonuclear DACs, while pairs of different metals are called heteronuclear DACs. In catalytic reactions, the metal pairs synergistically participate in the reactions. DACs are an extension of SACs, which not only have the advantages of SACs, but also introduce another degree of freedom for adsorption regulation of reaction intermediates, providing more possibilities for adsorption. At the same time, the interaction between bimetal sites can effectively regulate the activation energy and adsorption energy of reaction intermediates.[16] By further adjusting the number of central metal atoms, isolated active sites with three or four metal atoms called triatomic catalysts (TACs) or tetratomic catalysts can be obtained. The main advantage of such catalysts is the synergistic effect between multi-nuclear metals, providing a variety of reaction intermediates and transition states in catalytic reactions, searching for the optimal reaction path and the fastest reaction rate, which are more prominent for some complex multi-electron transfer processes.[17,18] At present, there are relatively few reports about the application of multi-atomic catalysts in electrocatalysis, although the research on SACs and DACs has achieved great progress. The study of catalysts at an atomic level opens a door to explore the relationship between activity and structure.

With the deepening of research, the electrocatalytic activity of atomic catalysts can be improved by adjusting the coordination structure of metal sites. Müllen *et al.* synthesized a P and N double-doped Fe single-atom catalyst (P/Fe–N–C) by introducing P atoms into the second coordination layer of Fe–N_4, which showed OER/ORR bifunctional activity. Theoretical calculations showed that P doping can adjust the *OOH/*O adsorption energy at the Fe–N_4 site and accelerate the reactions.[19] Liu *et al.* used a controlled "precursor preselection" strategy to synthesize a class of Cu and Co DACs with different coordination shells.[20] When Cu and Co metals bond to S, they have lower valence states, which are conducive to the ORR. However, when S is in the second shell and is coordinated with N, the metal atoms show an intermediate equivalent state, which is conducive to the OER. Additionally, when S is doped on the base surface it is far away from the metal, which is in a high valence state and is favourable for the HER.

In addition to SACs and DACs, the synthesis and characterization of TACs can be experimentally realized. However, TACs are still in the development stage, since the more central the metal atoms, the greater the probability of metal agglomeration, and the greater the challenge of synthesis. TACs have great potential to catalyse the conversion of CO_2 to C_2 and C_{2+} products due to multi-metal site synergistic catalysis. Using theoretical calculations, Dou *et al.* demonstrated that spatially confined three-centered metal atoms can simultaneously fix a few molecules of carbon dioxide and have multiple reaction paths, which are spatially and electronically conducive to the coupling of C–C and C_2–C to generate C_2 and C_3 products with high added-value.[21] On M_3@NG, the reaction steps of CO_2 → *COOH → *CO → *CHO → *CH are similar to those on copper catalysts, and the speed control step is *CO → *CHO. Then *CH can be converted into *CH_2 or *CH–CO, and the C–C coupling process of the latter can be carried out on the middle spatially confined trinuclear metal to form C_2 or continue coupling to produce C_3. This provides a new idea for designing novel electrocatalysts for CO_2 reduction to C_{2+} products. Zhang *et al.* reported a trinuclear nickel catalyst (TNC-Ni), where the interaction among the three nickel sites plays a key role in charge accumulation and O–O bond formation during water oxidation.[22]

About 297 million tons of nitrogen are annually converted by biological nitrogen fixation, in which dimeric enzyme complexes (FeMo, FeV, or FeFe active sites) play a catalytic role, effectively reducing the reaction energy barrier. However, the slow kinetics limits high yields, and the stability and recyclability of catalysts are challenging.[23–26] Inspired by natural nitrogen fixation, Ma *et al.* proposed a heteronuclear FeV@C_2N diatomic electrocatalyst, which effectively inhibited competitive HER and had good NRR activity and selectivity.[27] Dey *et al.* reported the synthesis of a trinuclear Ni complex (Ni_3S_8) using PhOH as a proton source, which selectively reduces N_2 to N_2H_4.[28]

In this review, we summarize the recent progress of atomic catalysts in the electrocatalysis of the HER, OER, ORR, CO_2RR and NRR, and a main development timeline of SACs, DACs and TACs is shown in Fig. 1. The regulation strategies of metal active sites are discussed, including reasonable design of substrates, regulating the electronic structure of central metal atoms and the coordination environment. Furthermore, the influencing factors of atomic catalysts for electrocatalysis are theoretically analysed and the strategy of optimizing the atomic catalyst is proposed. Finally, we put forward the current challenges and opportunities for future development of atomic catalysts to guide the reasonable design of multi-atomic catalysts in the future.

2. Reasonable control of the geometric and electronic structure of metal active sites

Geometric configuration and electronic structure are crucial for metal active sites towards advanced electrocatalysis.[39] The geometric configuration reflects the coordination environment between the active metal and the surrounding atoms, and the electronic structure of the active site is closely related to the coordination environment. When the distance between two metal atoms is less than 1.0 nm, the two metal atoms will interact and affect the distribution of electrons.[40] The selection and modification of the substrate also play an important role in the geometric configuration and electronic structure of central metal atoms, and the selection of special position on the substrate is beneficial to the formation of a unique electronic structure. The active center is composed of metal and coordination atoms, and the interaction between metal and metal/non-metal will cause charge rearrangement, and therefore, reasonable selection of the number and type of metal is very important to design catalysts with different electrocatalytic activities.[41] In this section, we first introduce the rational design of atomic catalysts with different numbers of metal nuclei through defect engineering and spatial limiting, and focus on

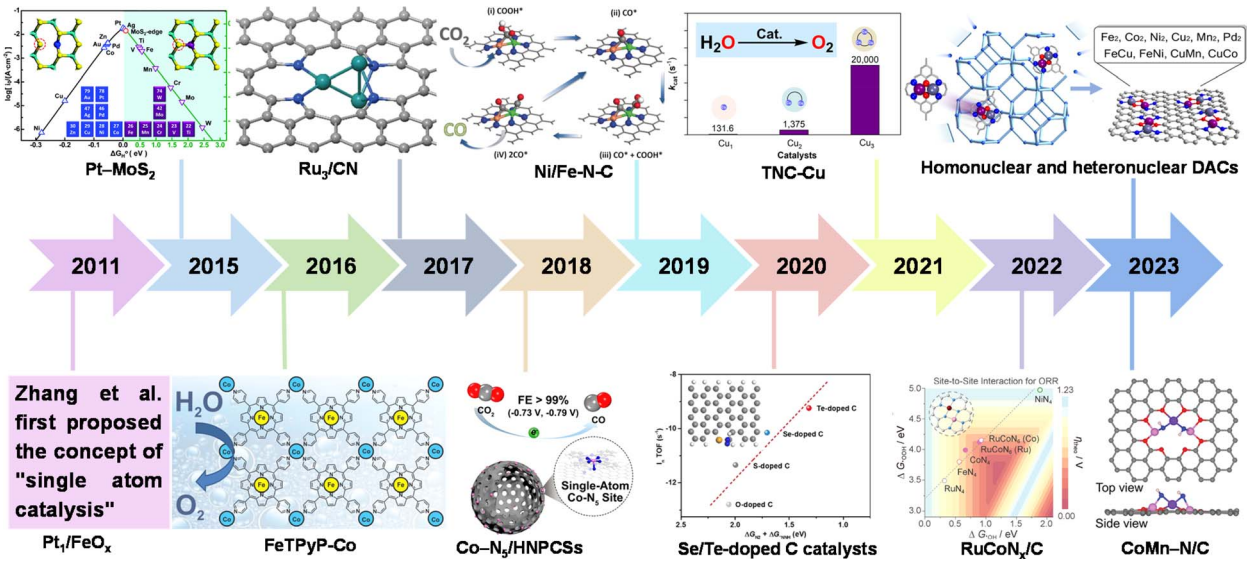

Fig. 1 History of catalysts with different nuclear numbers for electrocatalysis. Pt_1/FeO_x.[12] Pt–MoS_2. Reproduced with permission.[29] Copyright 2015, The Royal Society of Chemistry. FeTPyP-Co. Reproduced with permission.[30] Copyright 2016, American Chemical Society. Ru_3/CN. Reproduced with permission.[31] Copyright 2017, American Chemical Society. Co–N_5/HNPCSs. Reproduced with permission.[32] Copyright 2018, American Chemical Society. Ni/Fe–N–C. Reproduced with permission.[33] Copyright 2019, Wiley-VCH. Se/Te-doped C catalysts. Reproduced with permission.[34] Copyright 2020, Wiley-VCH. TNC-Cu. Reproduced with permission.[35] Copyright 2021, American Chemical Society. $RuCoN_x$/C. Reproduced with permission.[36] Copyright 2022, American Chemical Society. Homonuclear and heteronuclear DACs. Reproduced with permission.[37] Copyright 2023, American Chemical Society. CoMn–N/C. Reproduced with permission.[38] Copyright 2023, Wiley-VCH GmbH.

how to regulate the central metal atoms and the coordination environment.

2.1. Reasonable design of substrates

2.1.1. Defect engineering. Defect engineering can be adopted to regulate the electronic structure and surface morphology of catalysts by controlling the type, concentration and distribution of defect sites, so that the catalysts have unique physical and chemical properties to improve the catalytic activity. The defects in the substrate carbon materials mainly include intrinsic defects and externally induced defects. The intrinsic defects generally include pore, edge, vacancy and topological defects. The defects induced by external factors, such as N, P, S, B and F nonmetallic heteroatom doping and Fe, Co, Ni, Cu and Zn metal atom doping, are caused by the destruction of the original sp^2 carbon lattice of the carbon material by the bonding of carbon atoms with non-carbon atoms.[42–44] Yao *et al.* prepared a highly stable atomically dispersed Ni catalyst using defective graphene (A-Ni@DG) for the electrocatalytic OER and HER.[45] X-ray absorption spectroscopy (XAS) characterization and density functional theory (DFT) calculations showed that different defects within graphene can induce different local electron state densities of Ni species (Fig. 2).

Xu *et al.* reported a carbon-supported defect-anchored Pt SAC.[46] The ORR on the Pt SAC is a four-electron reaction with a high half-wave potential (0.835 V *vs.* RHE). Theoretical calculations showed that the Pt–C_4 site with two carbon vacancies is the active center of the ORR. Wang *et al.* constructed defect sites on TiO_2 nanosheets to stabilize single-atom Au sites, which can improve catalytic activity by reducing the energy barrier and competitive adsorption at isolated Au atomic sites.[47] Chen *et al.* prepared a catalyst with a copper atomic pair (Cu^0_1–Cu_1^{x+}) that was stabilized by Te surface defects on $Pd_{10}Te_3$ alloy nanowires. High FE (FE_{CO} = 92%) was shown for the CO_2RR, and the HER was almost completely suppressed.[48] Theoretical calculations showed that the Cu^0_1–Cu_1^{x+} site can promote CO_2 activation by the "diatomic activation bimolecular mechanism". Yao *et al.* reported a locally distributed atomic Pt–Co nitrocarbon-based catalyst (A-CoPt-NC) with 267 times higher mass ORR activity than commercial Pt/C.[49] DFT calculations showed that the high ORR activity is due to the synergistic interaction between Pt–Co atom pairs and the surrounding defective coordination environment, and the electron distribution of the Pt–Co active center is asymmetrical.

The introduction of nonmetallic heteroatoms such as P or S into the carbon carrier will cause the change of charge density of active sites due to the mismatch between the heteroatoms and the outer orbitals of carbon, thus regulating the electrocatalytic performance.[50,51] Deng *et al.* synthesized an N,P codoped FeNi-NPC catalyst with diatomic Fe–Ni sites, where P does not coordinate with the diatomic Fe–Ni site.[52] By adjusting the microenvironment and designing the structure, the catalytic OER/ORR activities of FeNi-NPC were effectively improved. Zou *et al.* synthesized a S-doped Mo single atom/carbon multichannel fiber catalyst (MoSA/CMF-S) using template assisted electrospinning.[53] The catalyst catalyzed the NRR to generate NH_3 with a yield of 46.6 μg h^{-1} mg_{cat}^{-1} and FE of 28.9% at −0.2 V. Theoretical calculations showed that the catalytic active site of MoSA/CMF-S is $Mo_1N_1C_2$–S4, where S does not

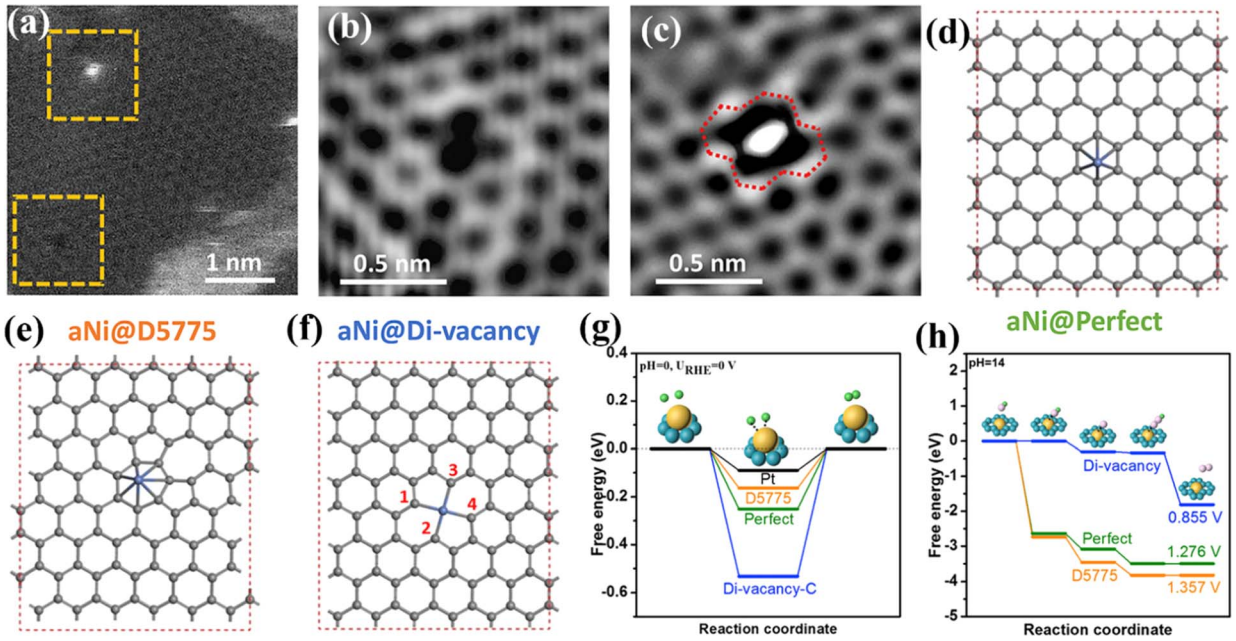

Fig. 2 (a–c) High angle annular dark field-scanning transmission electron microscopy (HAADF-STEM) images of A-Ni@DG. (d–f) Illustrations of three different types of catalytic active sites corresponding to a single Ni atom supported on (d) perfect hexagons, (e) D5775, and (f) di-vacancy. (g and h) Energy profiles of three configurations (d–f) for the HER (g) and OER (h). Reproduced with permission.[45] Copyright 2018, Elsevier.

coordinate with a Mo atom. Bader analysis showed that S doping makes the charge of the Mo atom rearrange. By comparing the charge of Mo in $Mo_1N_1C_2$–S4 and $Mo_1N_1C_2$, the charge of the Mo atom in the former increases more than that in the latter, and a charge accumulates between S and Mo in the $Mo_1N_1C_2$–S4. In addition, HER kinetics was slow at the $Mo_1N_1C_2$–S4, indicating that S doping effectively inhibited the HER. The adsorption energy of N_2 on the side-on (−0.87 eV) and end-on (−0.82 eV) orientations of a single Mo atom at the active site was calculated. The adsorption energy of N_2 at the $Mo_1N_1C_2$–S4 site was −0.88 eV, which is stronger than that at $Mo_1N_1C_2$ (−0.79 eV). In addition, the speed control step at the $Mo_1N_1C_2$–S4 (0.58 eV) is easier to overcome than that at $Mo_1N_1C_2$ (0.81 eV) (Fig. 3). In short, the introduction of S rearranges the electrons of single-atom Mo, which is conducive to the adsorption of N_2 and effectively inhibits HER activity.

2.1.2. Spatial confinement. Atomic confinement can be divided into chamber confinement and grid confinement. Chamber confinement is generally achieved by confining isolated transition metal precursors in a stable structure, such as the encapsulation of cobalt acetyl acetone in a chamber of imidazole molecular sieve framework, which requires the size of metal precursors and the cavity.[54] For grid confinement, metal atoms are stabilized by forming strong coordination and covalent bonds, such as metal porphyrins and metal phthalocyanines in covalent organic frameworks (COFs). It is needed to ensure that the small molecules have symmetry in order to obtain a periodic framework.[55,56] By separating and encapsulating suitable mononuclear metal precursors in porous materials such as zeolites, metal organic frameworks (MOFs), and COFs, the finite dispersion of atoms is achieved.[57–60]

Li *et al.* used cage encapsulation and pyrolysis strategies to obtain a single-atom iron catalyst with good ORR activity, exhibiting a half-wave potential of 0.9 V in 0.1 M KOH and good stability.[61] DFT calculations showed that the good ORR activity is attributable to the formation of single-atom Fe, which coordinates with four N atoms and is axially adsorbed with O_2 (Fig. 4a). Li *et al.* packaged a W precursor into a MOF and pyrolyzed it to obtain a W single-atom catalyst with a local structure of $W_1N_1C_3$.[62] The catalyst showed good HER activity with an overpotential of 85 mV at 10 mA cm^{-2} (η_{10}) in 0.1 M KOH. Huang *et al.* prepared an ultra-stable bimetallic phthalocyanine COF (Fig. 4b).[63] The overlap stacking mode of metal phthalocyanine units is conducive to electron transfer and improves the FE of CO_2 conversion to CO (FE = 97%). Niu *et al.* used encapsulation and pyrolysis strategies to construct a series of diatomic catalysts, including homo-nuclear (Fe_2, Co_2, Ni_2, Cu_2, Mn_2 and Pd_2) and hetero-nuclear (Fe–Cu, Fe–Ni, Cu–Mn and Cu–Co) DACs.[37] After pyrolysis, the molecular skeleton of macrocyclic complexes can be preserved (Fig. 4c). Taking Fe–Cu DAC as an example, it showed good ORR activity ($E_{1/2}$ = 0.793 V) and stability. Besides the above two atomic confinement methods, Zhang *et al.* designed a click-limiting strategy to disperse cobalt-coordinated porphyrin units onto the substrate to obtain a Co–N–C electrocatalyst, which showed excellent OER/ORR activities (ΔE = 0.79 V) (Fig. 4d–f).[64]

2.2. Regulating the electronic structure of central metal atoms

The electronic structure of central metal atoms plays an important role in optimizing the physical and chemical properties of catalysts. The central metal atom determines the

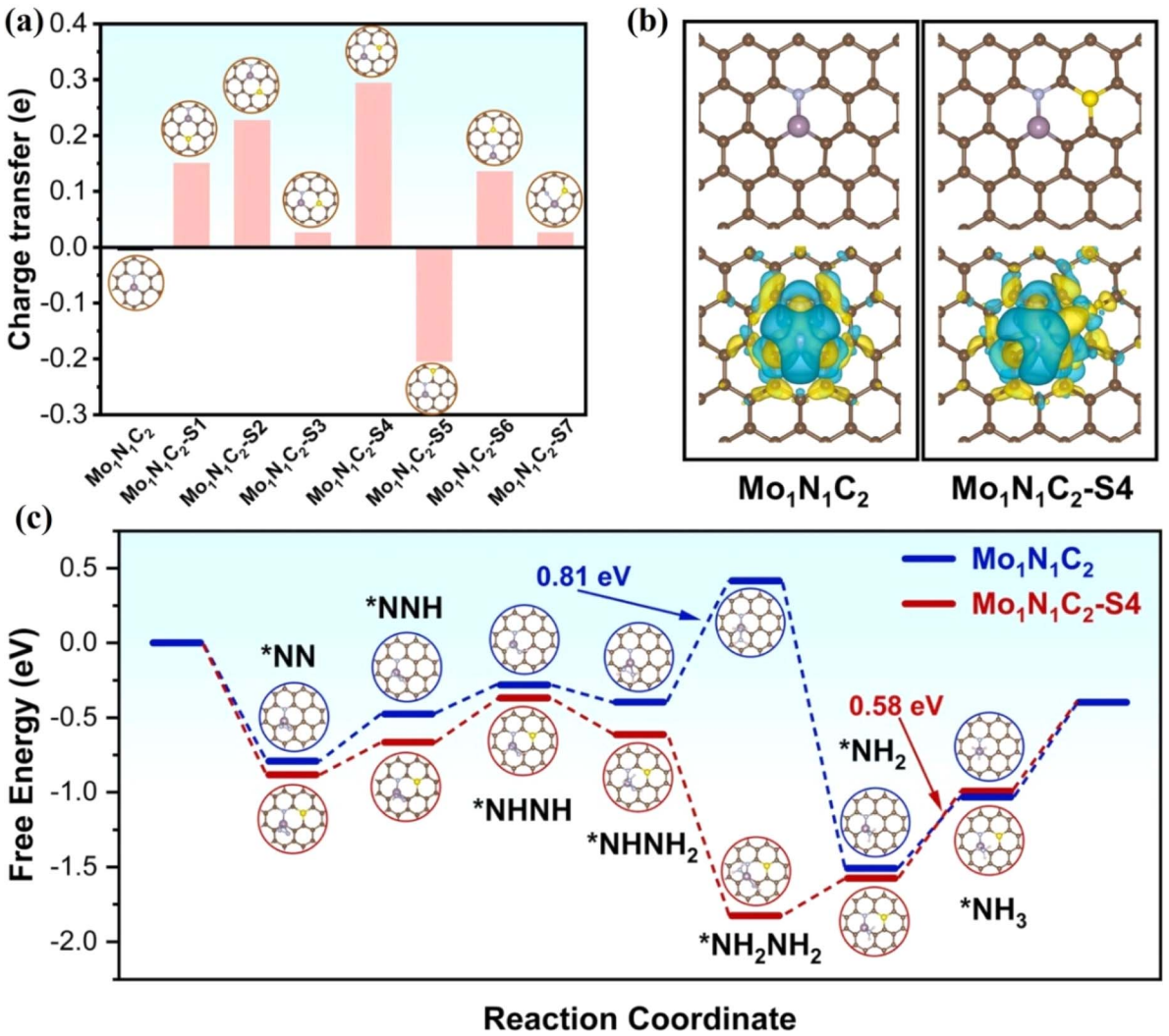

Fig. 3 (a) Bader charge variations of the Mo atom in different S-doped samples. (b) Optimized geometries and contour plots of the charge density differences. (c) Gibbs free energy diagram of enzymatic NRR. Reproduced with permission.[53] Copyright 2022, Elsevier B.V.

energy level of the d orbital, the number of d electrons and the electron configuration. The distance between metal centers and the combination of metal centers are important factors affecting chemical reactions.[65–67] Single, double and triple metal atoms with isolation are obtained by adjusting the distance of metal centers, namely SACs, DACs and TACs, respectively (Fig. 5). The charge distribution between the active sites is optimized by adjusting metal combination, thereby changing the electronic properties of the metal atoms. The electronic structure of the central metal atom determines the atomic charge distribution and Fermi level, thus influencing the adsorption/desorption energy of reaction intermediates.[68] In this section, we will discuss how to adjust the electronic structure of the central metal atoms of SACs, DACs and TACs.

2.2.1. Regulating the electronic structure of SACs. The development of SACs has opened a new door for heterogeneous catalysis. SACs have single isolated active sites, high metal utilization and unique electronic structure. The optimized electronic structure of the active center and the surrounding unsaturated coordination environment can increase electrocatalytic performance. SACs have become an ideal system for the study of catalytic mechanisms by combining theory and experiment, further guiding the design of new catalysts.

Hydrogen production by electrolysis of water is a green and sustainable method, which is expected to replace fossil fuels in the future. Precious metal platinum-, palladium-, and iridium-based catalysts play an important role in water electrolysis. However, Pt, Pd and Ir have small reserves and high costs, which are obstacles in large-scale electrocatalytic hydrogen production.[69] At present, ideal electrocatalysts can be developed by two strategies, one is to prepare SACs with fewer precious metals, and the other is to develop non-precious metal catalysts.[70,71] In the HER, there are three basic steps: Tafel, Heyrovsky, and Volmer, where the Volmer step is the fastest and Tafel is the rate-determining step. The formation and desorption processes of the reaction intermediate H* affect the reaction mechanism and reaction rate. According to Sabatier's

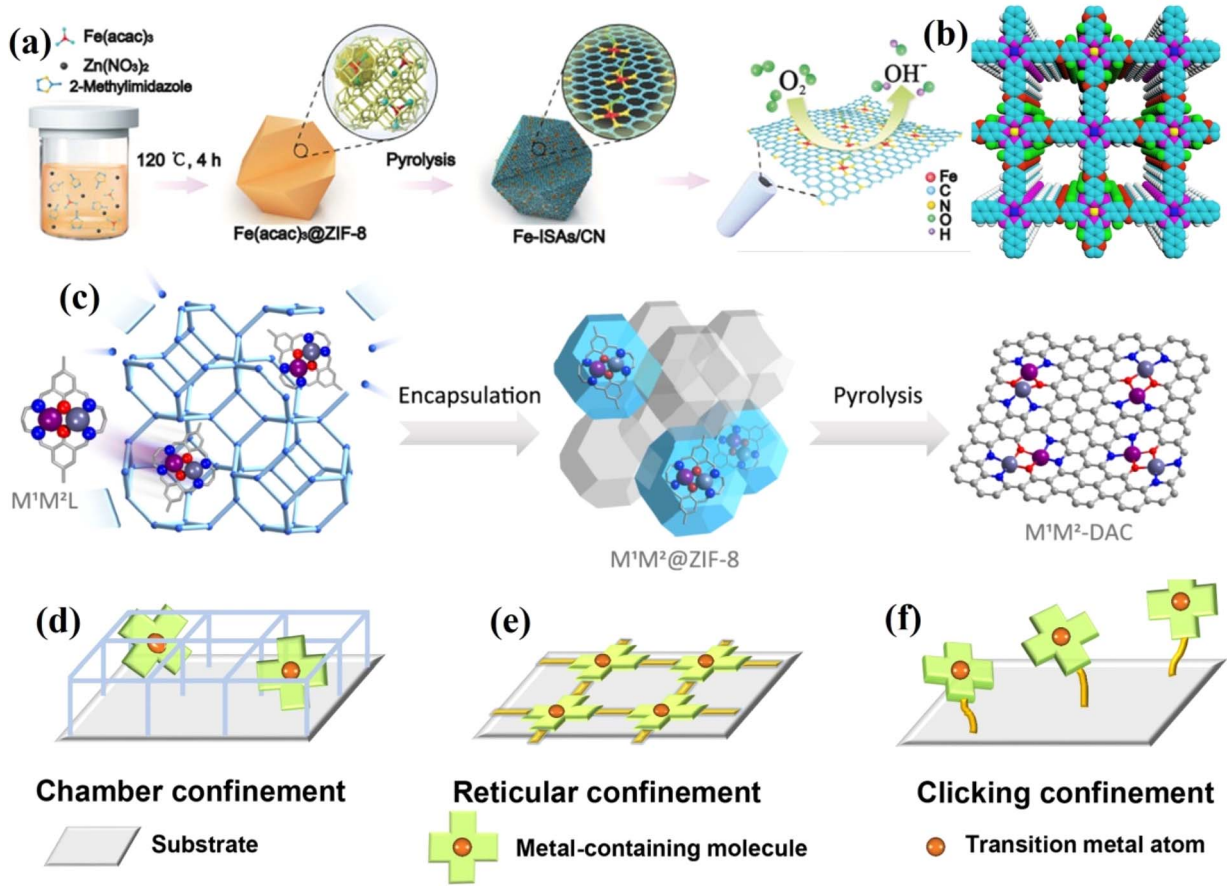

Fig. 4 (a) Schematic illustration of the formation of Fe-ISAs/CN. (b) Top views of a graphical representation of the eclipsed stacking of $CuPcF_8$-CoNPc-COF. (c) Schematic illustration of the synthesis of DACs *via* a macrocyclic precursor-mediated encapsulation–pyrolysis process. (d–f) Different confinement strategies for fabricating M–N–C SACs. (a) Reproduced with permission.[61] Copyright 2017, Wiley-VCH. (b) Reproduced with permission.[63] Copyright 2021, American Chemical Society. (c) Reproduced with permission.[37] Copyright 2023, American Chemical Society. (d–f) Reproduced with permission.[64] Copyright 2022, American Association for the Advancement of Science.

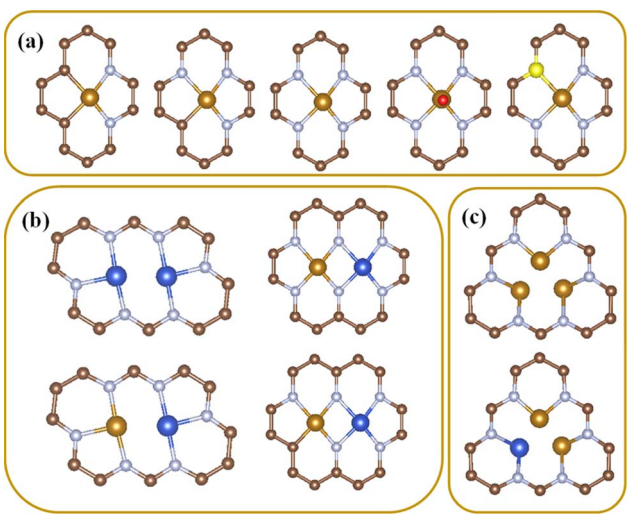

Fig. 5 (a–c) Typical structures of SACs, DACs and TACs.

principle, when the hydrogen adsorption free energy G_{H^*} is close to 0, the HER is the most favourable to occur. Under alkaline conditions, the activity of the HER is also affected by the kinetic energy barrier of water splitting and the energy barrier of hydroxyl desorption.[72]

For the HER, Pt-based catalysts are the most active electrocatalysts. Lee *et al.* loaded Pt onto low-oxide tungsten (Pt SA/WO_{3-x}), which greatly improved the utilization of Pt, and demonstrated that Pt SA/WO_{3-x} was significantly superior to WO_{3-x} loaded with Pt nanoparticles (Pt NP/WO_{3-x}).[73] At an overpotential of 50 mV, the mass activity of Pt SA/WO_{3-x} was 10.7 times that of Pt NP/WO_{3-x}. In practical applications, pH has a great effect on HER activity. Single-atom Pt catalysts show good performance under different pH values. Tan *et al.* modified Pt atoms into nanoporous $Co_{0.85}Se$ (Pt/np-$Co_{0.85}Se$), and the catalyst showed excellent HER activity under neutral conditions, with an initial potential close to 0 and a Tafel slope of 35 mV dec^{-1}.[74] Operando XAS and theoretical calculations showed that Pt in Pt/np-$Co_{0.85}Se$ can not only regulate the surface state of the active center, but also decrease the ΔG of the HER, optimize the hydrogen adsorption/desorption energy, and promote thermodynamics and kinetics.

Compared with acidic conditions, the HER rate and apparent activity of catalysts is slower under alkaline conditions, and thus it is relatively difficult to design atomic catalysts

that can catalyse the HER under alkaline conditions. The π-electron hybridization at the edge of the carrier graphene is used to influence the electronic state of the Pt 5d orbital. Amal *et al.* used edge-rich vertical graphene to anchor Pt, and Pt coordinated with the graphene edge showed excellent HER activity with a turnover frequency (TOF) up to 22.6 s^{-1} at η = 150 mV.[75]

The anchoring of single-atom platinum to a suitable carrier can facilitate the HER due to the optimization of metal–carrier interaction and water adsorption. Jiang *et al.* anchored single-atom Pt to α-MoC_{1-x}@C (Pt_{SA}/α-MoC_{1-x}@C), which showed high activity and stability for the pH-universal HER.[76] The η_{10} of Pt_{SA}/α-MoC_{1-x}@C under alkaline and acidic conditions is 21 mV and 12 mV, respectively. X-ray photoelectron spectrometry (XPS) and XAS analysis indicated that Pt in Pt_{SA}/α-MoC_{1-x}@C is present in a low state, which is caused by electron migration from Mo to Pt. Experimental results showed that platinum atoms are monodispersed in the α-MoC_{1-x}@C lattice. DFT analysis showed that the ΔG of hydrogen adsorption decreases significantly (0.60 eV → 0.21 eV) with the construction of the Pt unit point under acidic conditions, which is favourable for hydrogen adsorption/desorption. Under neutral and alkaline conditions, α-MoC_{1-x}-Pt is beneficial to water adsorption, promotes the capture of reactants, and accelerates the HER. In addition, the hydroxide adsorption free energy is reduced on α-MoC_{1-x}–Pt, and the interaction between α-MoC_{1-x} and Pt atoms optimizes the adsorption/desorption energy of reaction intermediates. Thus, Pt_{SA}/α-MoC_{1-x}@C showed pH-universal HER activity (Fig. 6).

In addition to the precious metal Pt, transition metal cobalt and nickel-based catalysts are used to catalyse the HER in acidic environments.[77–80] Studies have shown that transition metal carbides have a low energy barrier in hydrogen adsorption, and the density of states near the Fermi level is similar to that of precious metals. Nickel carbide (NiC) shows stability in a wide pH range. By introducing N into NiC, the electronic structure of Ni can be adjusted to improve the HER activity. In addition, the conductivity of the catalyst can be improved by reducing its size. Sun *et al.* prepared hybrid Ni–C–N nanosheets with thickness smaller than 2 nm.[81] Ni–C–N is chemically stable and has metal conductivity, which showed good HER activity in 0.5 M H_2SO_4, 1.0 M KOH and 1.0 M PBS (pH = 7). Yu *et al.* prepared nitrogen-

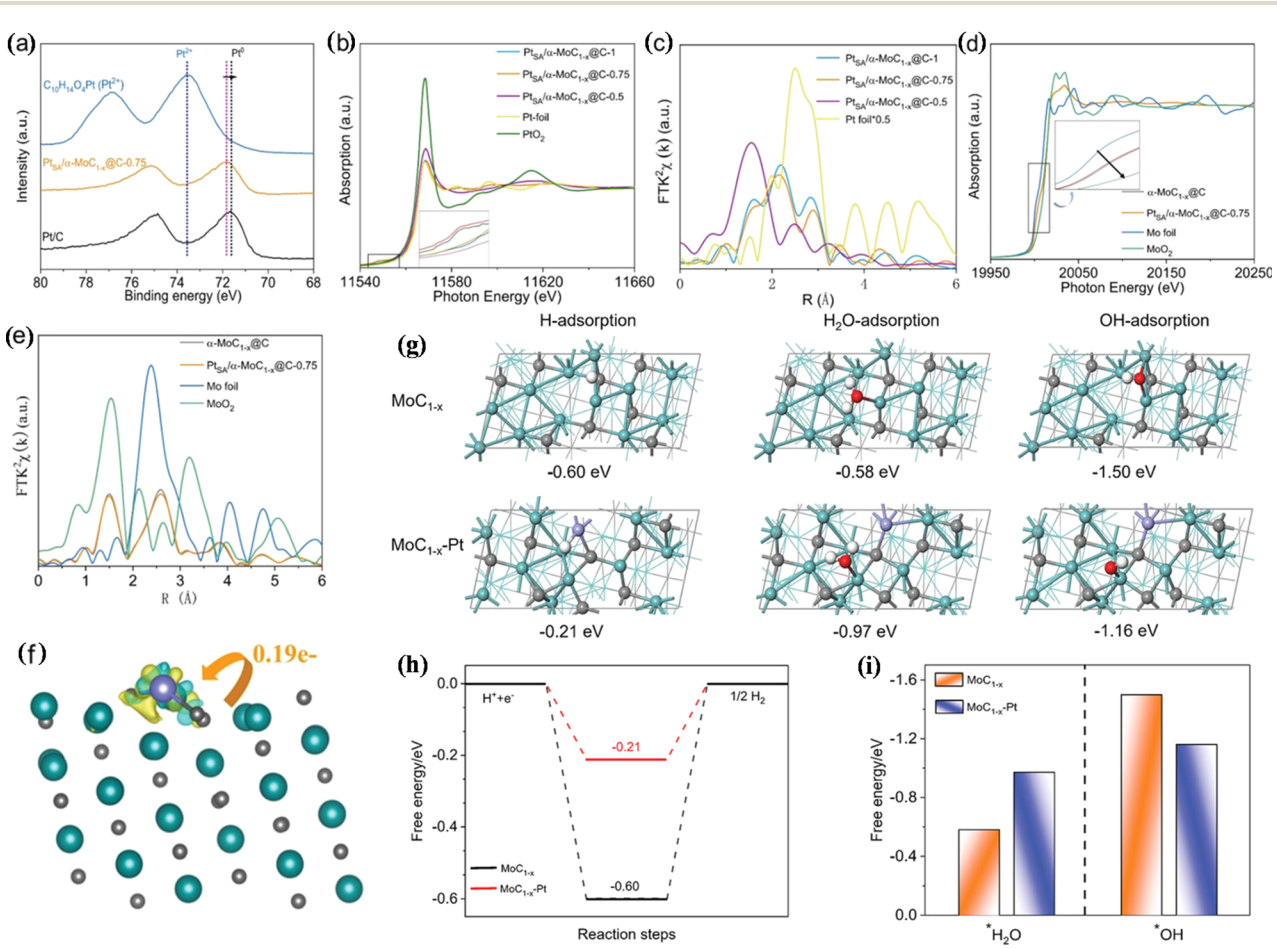

Fig. 6 (a) Pt 4f XPS spectra. (b) Pt L_3-edge XANES spectra. (c) Fourier transform X-ray absorption fine structure (FT-EXAFS) curves. (d) Mo K-edge X-ray absorption near edge structure (XANES) spectra. (e) FT-EXAFS curves of the Mo K-edge. (f) Differential charge density for Pt_1/α-MoC_{1-x}. (g) Optimized adsorption geometries. (h) Gibbs free energy diagram. (i) Calculated adsorption free energies. Reproduced with permission.[76] Copyright 2021, Wiley-VCH GmbH, Weinheim.

doped porous nanofibers with Fe–N_5 sites (Fe SA/PNCNFs-0.1) by a wet impregnation method.[79] The catalyst showed a high catalytic HER activity with an η_{10} of 44.3 mV and Tafel slope of 45.4 mV dec^{-1}. However, there are still some issues in transition metal catalysts catalysing the HER at full pH, because the process will cause the change of proton concentration. To make water splitting more energy-saving, the ideal state should show excellent activity at any pH.

The OER is a complex four-electron process whose reactivity determines the efficiency of hydrogen production by water electrolysis.[82] At present, the most advanced OER electrocatalysts are IrO_2 and RuO_2, but they have poor stability in alkaline media.[83] SACs have attracted much attention because of their unique electronic structure.[84] By anchoring precious metals to supports, SACs can be prepared to reduce the use of precious metals while ensuring high OER activity. Huang *et al.* prepared single-atom Rh-doped CuO nanowires on a copper foam (Rh SAC-CuO NAs/CF) using a cation exchange strategy, which exhibited an η_{10} of 357 mV for the OER.[85] Theoretical calculations showed that the introduction of Rh atoms into the CuO lattice can effectively reduce the reaction energy barrier and accelerate the kinetics. Gu *et al.* synthesized a single-atom iridium-doped nickel phosphide catalyst (Ir_{SA}-Ni_2P) using a top-down phosphating strategy, which showed excellent OER activity with an η_{10} of 149 mV.[86] Simulated results of Ir_{SA}-$Ni_{12}P_5$ and Ir_{SA}-Ni_2P nanospheres showed that iridium atoms replace the outermost nickel and occupy the Ni sites in the Ni_xP_y (Ni_2P and $Ni_{12}P_5$) matrix (Fig. 7).

In addition, the abundant and inexpensive transition metals Mn, Fe, Co and Ni are often used as active centers of SACs for the OER.[87] Kibria *et al.* synthesized a cobalt-anchoring nitrogen-rich carbon single-atom catalyst (Co SAC) with a Co loading content of 10.6 wt% using a macromolecular assisted strategy.[88] The Co SAC had an OER η_{10} of 351 mV under alkaline conditions and a mass activity of 2209 mA at 1.65 V, and showed tolerance for up to 300 h. According to operando XAS analysis, the pyridine nitrogen in a cobalt phthalocyanine tetramer (CoPc) with melem (CoMM) was suitable for the OER and had good reproducibility. Close Co–Co atomic spacing (~3.85 A) and e_g packing can increase OER activity. In addition, theoretical calculations showed that electron-deficient Co–O coordination intermediates are easily formed to accelerate the reaction kinetics, and the Co–N_4 coordination structure can effectively reduce the reaction energy barrier and increase the OER activity (Fig. 8). According to the Sabatier principle, a good catalyst should optimize the adsorption energy of reaction intermediates. The OER involves adsorption and desorption of three reaction intermediates (*OH, *O and *OOH). Therefore, for a catalyst with high OER activity, the binding strength of the three intermediates to the active site should be moderate. Therefore, regulating the electronic structure and coordination environment of the active sites plays an important role in improving OER activity.[89–91]

The ORR plays an important role in energy storage and chemical production, such as in fuel cells, metal air batteries and hydrogen peroxide synthesis. However, these devices are faced with the problems of low ORR efficiency and slow dynamics.[92–96] According to the volcanic curve (Fig. 9a), metals with slightly lower oxygen binding energy than platinum have higher oxygen reduction rate, and transition metals Fe, Co, Ni

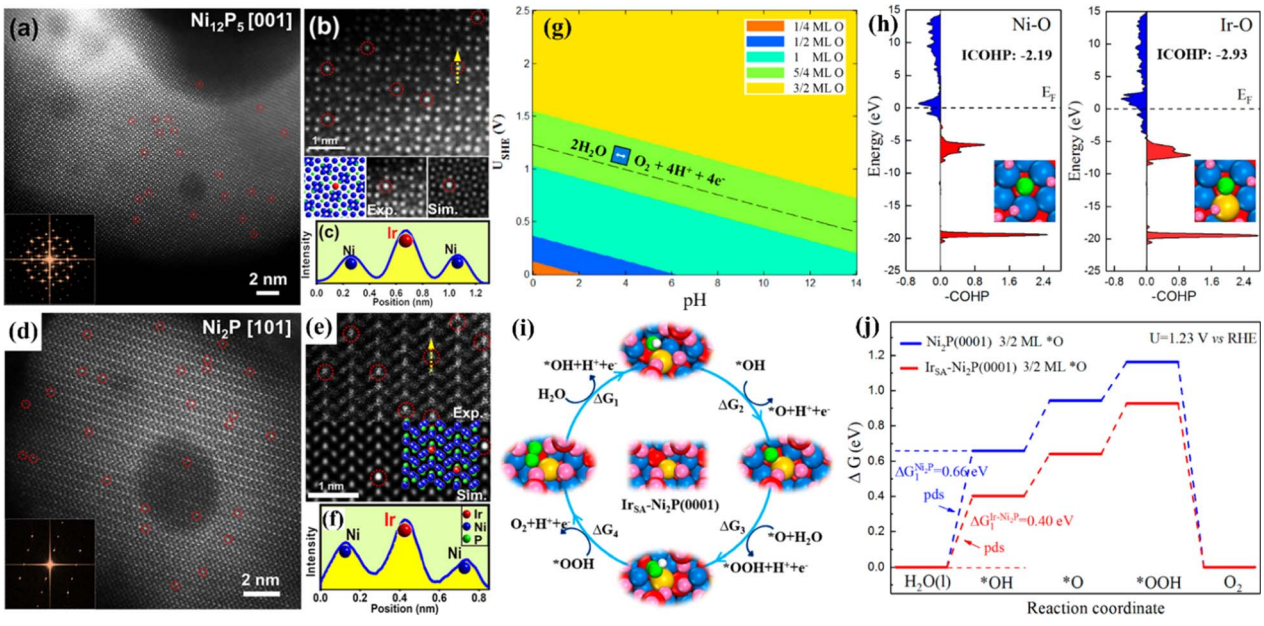

Fig. 7 (a and d) HAADF-STEM images and corresponding FFT (inset). (b and e) Experimental and simulated HAADF-STEM images. (c and f) Intensity profile of the yellow line in (b and e) with the matrix Ni column and the decorated Ir atom. (g) Surface Pourbaix diagram of a single Ir atom doped Ni_2P (0001) surface (Ir_{SA}-Ni_2P (0001)). (h) Projected crystal orbital Hamilton populations (COHP) between chemisorbed *O and active metal centers on Ni_2P (0001) and Ir_{SA}-Ni_2P (0001). (i) The optimized OER intermediates on Ir_{SA}-Ni_2P (0001). (j) Free energy diagrams. Reproduced with permission.[86] Copyright 2021, American Chemical Society.

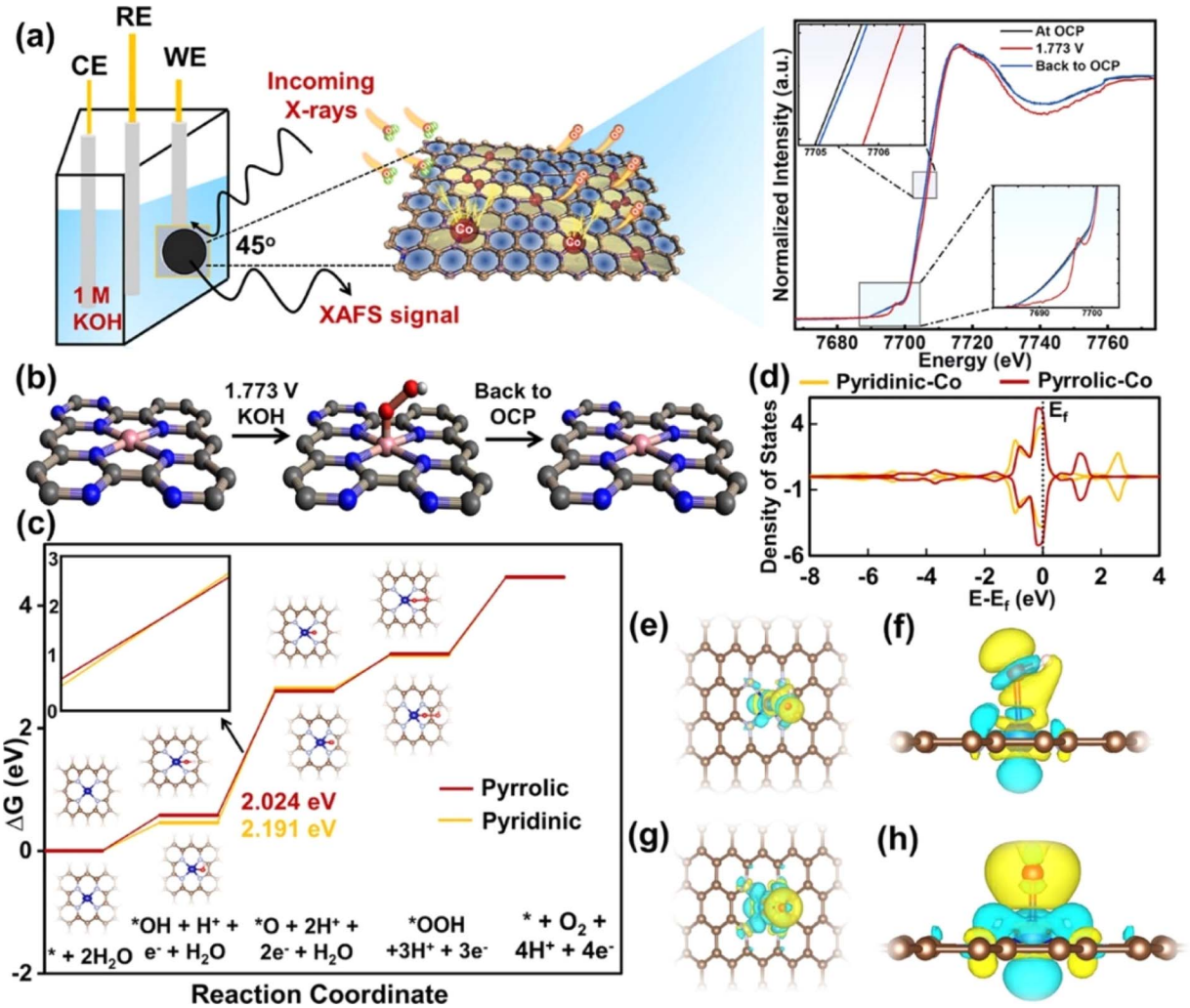

Fig. 8 (a) Schematics of operando XAS analysis of CoMM. (b) Chemical state change of CoMM during the OER. (c) OER free energy profile of pyridinic-nitrogen–cobalt and pyrrolic-nitrogen–cobalt single-atom models. (d) Projected density of states (PDOS) on the Co atom for both pyridinic-nitrogen–cobalt and pyrrolic-nitrogen–cobalt single-atom models. (e) Top view and (f) side view of *OH. (g) Top view and (h) side view of *O. Reproduced with permission.[88] Copyright 2023, American Chemical Society.

and Cu exhibit weaker binding energy of reaction intermediates. Anchoring them in the form of single atoms into conductive supports can promote the inherent ORR activity.[97,98] Zhang *et al.* synthesized an iron-doped mesoporous nitrogen-doped carbon material (Fe SAC-MIL101-T).[99] When the pyrolysis temperature was 1000 °C, the ORR activity was the best, and the half-wave potential was 0.94 V. The excellent ORR activity was attributed to the high dispersion of FeN_x active centers and abundant pore structure, which was conducive to mass transfer and improved the utilization rate of FeN_x active sites.

The strong binding of Co-based SACs with oxygen can promote a two-electron process in the ORR, which is conducive to the generation of H_2O_2. Co-based SACs with Co–N_4 structure like cobalt phthalocyanine and cobalt porphyrin are conducive to the $4e^-$ transfer process. However, when the cobalt is coordinated with five nitrogen atoms (Co–N_5), it shows high selectivity of H_2O_2.[100–104] Shao *et al.* used a coordination engineering strategy to prepare a Co single-atom catalyst with Co–N_5 sites (Co SAC), which had a good selectivity for H_2O_2 in the ORR.[105] The Co SAC demonstrated the two-electron process of the ORR in seawater with fast kinetics and chloride ion tolerance. The FE of H_2O_2 in 0.5 M NaCl solution with pH = 7 is as high as 95.6%. Theoretical calculation results showed that the ORR barrier of the two-electron pathway on the Co–N_5 is lower than that of the four-electron transfer process, and the Co–N_5 is more conducive to the activation and reduction of $*O_2$ than Co–N_4 (Fig. 9b–j).

In the CO_2RR, most metal-based SACs can reduce CO_2 to CO, and Sn- and Bi-based SACs can convert CO_2 to HCOOH, while Cu-based catalysts with moderate adsorption strength of CO_2 can reduce CO_2 to C_1, C_2 and C_{2+} products.[106–113] Cu is the only metal reported to be able to convert CO_2 into C_2 and C_{2+} products with high added value.[14,114] Chen *et al.* studied a series of TM-phthalocyanine (TM-Pcs, TM = Fe, Co, Ni, Cu, and Zn) crystal molecular catalysts with TM-N_4 active sites for the CO_2RR and revealed that the binding strength of the metal to reaction intermediates determines the activity of the CO_2RR.[115]

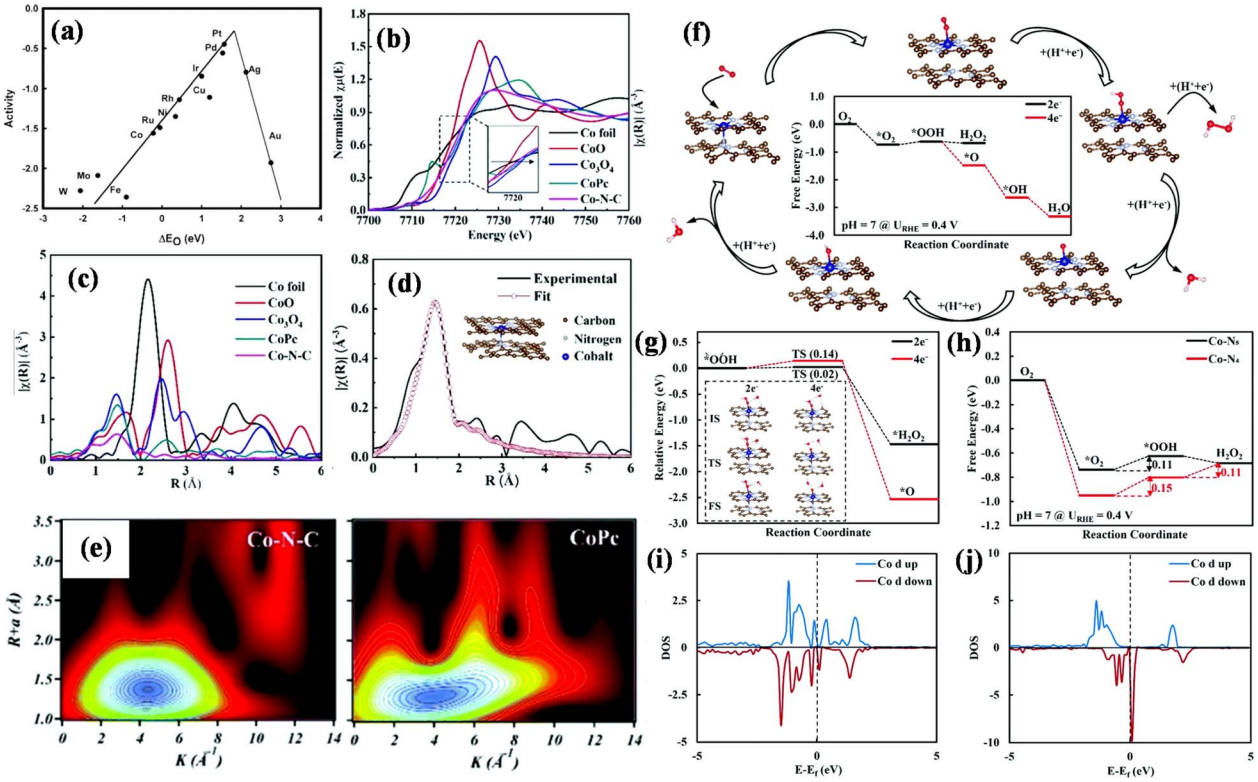

Fig. 9 (a) Trends in oxygen reduction activity plotted as a function of the oxygen binding energy. (b) The normalized K-edge XANES spectra and (c) FT-EXAFS spectra. (d) FT-EXAFS fitting curve of Co–N–C in *R* space and (e) wavelet transform (WT) for the k^3-weighted EXAFS signals. (f) ΔG diagram. (g) Kinetic energy barriers. (h) ΔG diagram of the two-electron transfer ORR pathway. (i) PDOS in Co–N_5 near the Fermi level (E_f). (j) PDOS in Co–N_4 near E_f. Reproduced with permission.[97] (a) Copyright 2004, American Chemical Society. (b–j) Reproduced with permission.[105] Copyright 2021, The Royal Society of Chemistry.

Shen *et al.* synthesized a series of M–N–C SACs (M = Fe, CO, Ni and Cu) by a leaching method.[116] The FE of CO on Ni–N–C reached up to 97%, and the activity of the CO_2RR was affected by the d-orbital electron configuration of the central metal ion. As shown in Fig. 10a–h, during the activation process, CO_2 interacts with the active site, and electrons are transferred from CO_2 to the active center metal, and then fed back to the π orbital of CO_2. Ni–N–C has higher electron density around Ni than other M–N–C because the outermost d orbital of Ni^{2+} is empty, which is conducive to the transfer of electrons from the C atom in the CO_2 molecule to the outermost orbital of the Ni atom and promotes the progress of the CO_2RR. Theoretical calculations showed that the rate-determining step of Ni–N–C is the formation of the *COOH intermediate, and the energy barrier of the rate-determining step on Fe–N–C, Co–N–C and Cu–N–C in the CO_2RR is greater than that in the HER, which is not conducive to the progress of the CO_2RR (Fig. 10i and j). Crystal field theory showed that the outermost space orbital of Ni^{2+} in the Ni–N–C is beneficial to the transfer of electrons from CO_2 to the active site Ni, effectively activating CO_2 molecules adsorbed on the surface.

Cu-based catalysts can induce CO* dimerization in the CO_2RR to obtain C_2 and C_{2+} products. The activity and selectivity can be improved by modifying the surface/interface of catalysts, such as adjusting the morphology, ligand modification, vacancy fabrication and doping. Han *et al.* applied a site-specific underpotential electrochemical deposition (UPD) strategy to treat single-atom Cu-anchoring Ag_2S/Ag nanowires.[117] Cu/Ag(S) was synthesized through single atom Cu occupying the defect position after sulfur removal. The FE of C_{2+} on Cu/Ag(S) is significantly higher than that on the Ag(S) catalyst without single-atom Cu, and Cu/Ag(S) showed the maximum FE (17%) at 1.4 V. Theoretical calculations showed that the interaction between Cu and Ag on the surface defects causes the d-band center to shift down, reduces the energy barrier of *CO formation (~0.5 eV), promotes the adsorption of reaction intermediates, and improves the selectivity of C_{2+}.

Ammonia (NH_3) is an important energy carrier and an important raw material for the synthesis of agricultural fertilizers. At present, NH_3 is industrially produced by the Haber–Bosch method, which needs high temperature and pressure. The conditions are harsh and the energy input is not in line with the trend of green and low-carbon development. The electrocatalytic NRR has attracted much attention because of its low energy consumption and mild reaction conditions. However, the NRR is a six-electron-proton transfer process with complex intermediates and slow kinetics. In addition, side reactions can occur through a two-electron pathway to diazene (N_2H_2) and four-electron pathway to hydrazine (N_2H_4). Therefore, in recent

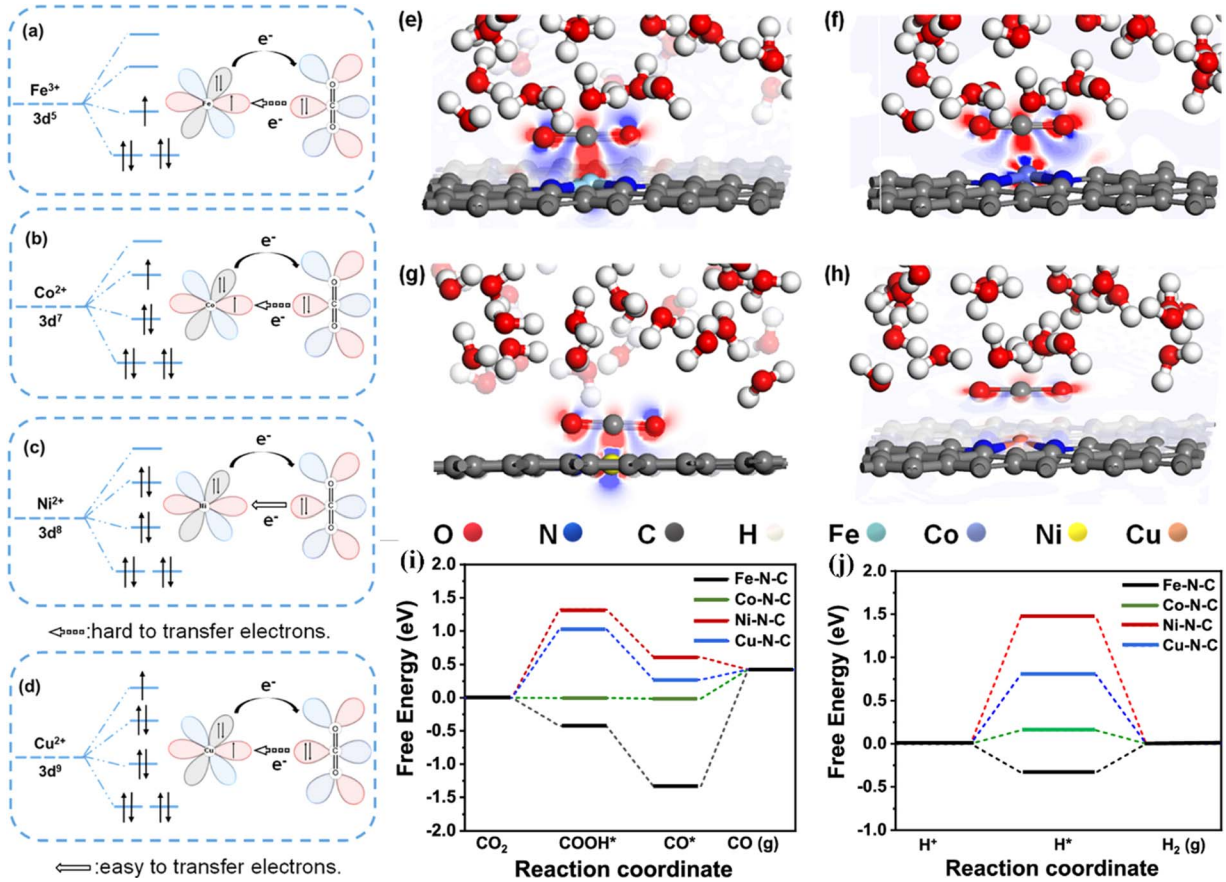

Fig. 10 Schematics of d-orbital electronic configurations of central metals in (a) Fe–N–C, (b) Co–N–C, (c) Ni–N–C, and (d) Cu–N–C and their electronic interaction with CO_2 molecules. Side-view differential charge density maps of (e) Fe–N–C, (f) Co–N–C, (g) Ni–N–C, and (h) Cu–N–C. The blue and red regions represent net electron accumulation and depletion, respectively. Reaction pathways and free energy diagrams of (i) the CO_2RR and (j) HER over M–N–C SACs at 0 V *versus* RHE. Reproduced with permission.[116] Copyright 2023, American Chemical Society.

years, the development of SACs with high activity and selectivity for the electrocatalytic NRR has been on the rise.[118,119]

Since the active metal center of the natural nitrogenase is Mo, it has been inferred that single-atom Mo catalysts might be efficient for the NRR. Xin *et al.* synthesized a single-atom Mo-anchoring nitrogen-doped porous carbon material (SA-Mo/NPC), showing an FE_{NH3} of 14.6 ± 1.6%.[120] NH_3 yields reached up to 34.0 ± 3.6 μg h^{-1} $mg_{cat.}^{-1}$, and SA-Mo/NPC was well tolerated in the NRR (Fig. 11a–g). Zhang *et al.* simulated a monatomic Mo-anchoring C_9N_4 catalyst (Mo@C_9N_4) for the NRR.[121] The results showed that the Mo atom is the active center of the NRR, and N_2 can be efficiently converted to NH_3 on the surface of Mo@C_9N_4. By comparing the remote and alternate pathways, the energy barrier (0.40 V) of the rate control step of $*N_2 \rightarrow *N_2H$ in the remote pathway is lower than that (0.70 V) of the rate control step of *NNH → *NHNH in the alternate pathway. Through the analysis of the bond length and charge changes in each step of the NRR, it was concluded that single-atom Mo serves as both the reservoir and the electron transfer transmitter between the intermediate $*N_xH_y$ and the carrier C_9N_4 in the NRR process (Fig. 11h–k).

2.2.2. Regulating the electronic structure of DACs. A DAC refers to a catalyst with metal dimers on the substrate. The interaction between two adjacent active metal sites redistributes electrons, which is conducive to improving the catalytic performance, and catalysing complex reactions involving multiple reactants, reaction intermediates and products. According to the kind of active metal center, DACs are divided into homonuclear DACs and heteronuclear DACs.

2.2.2.1. Homonuclear DACs. Homonuclear DACs can be obtained by increasing metal loadings. Compared with SACs, the active sites of DACs increase due to the increase in the metal loadings.[122] In addition, the interaction between homonuclear metals can regulate the electronic structure of active centers, which is conducive to reducing the reaction energy barrier. Zhou *et al.* constructed a diatomic Ag/graphene with AgN_3–AgN_3 structure (Ag_2–G), which showed good activity in catalysing the conversion of CO_2 to CO, with an FE of up to 93.4%.[123] Theoretical calculations showed that the AgN_3–AgN_3 active site has a lower energy barrier of *COOH formation than single-site Ag_1–G. Wang *et al.* reported a diatomic Pd catalyst (Pd_2 DAC) for the CO_2RR, exhibiting an FE_{CO} of 98.2%.[124] DFT calculations unveiled that the enhanced activity of the CO_2RR is due to the electron transfer between Pd and Pd, optimizing the adsorption strength of the reaction intermediate CO*. Quan *et al.* synthesized a nitrogen-coordinated Fe DAC (Fe_2NPC) using $Fe_2(CO)_9$

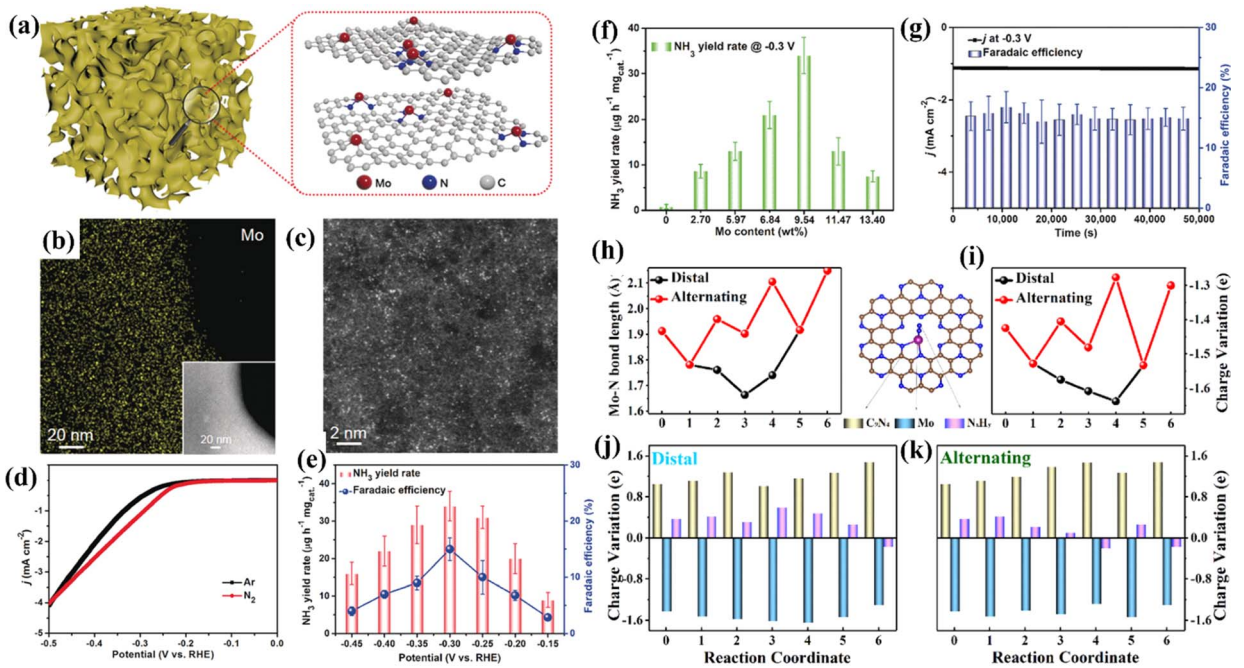

Fig. 11 (a) Illustration of SA-Mo/NPC. (b) Mo EDS mapping. (c) HAADF-STEM image. (d) LSV curves. (e) NH_3 yield rate and FE at each given potential. (f) NH_3 yield rates with different Mo loadings. (g) Chronoamperometric curve and FE stability. (h) Mo–N bond length during the NRR process. (i) Charge variation of a single Mo atom during the NRR process. Charge variation of the three moieties (C_9N_4, single Mo atom and the adsorbed N_xH_y species) along (j) distal and (k) alternating pathways. (a–g) Reproduced with permission.[120] Copyright 2019, Wiley-VCH. (h–k) Reproduced with permission.[121] Copyright 2020, Elsevier B.V.

as the Fe source, exhibiting an FE_{CO} of 96.0%.[125] XAS characterization showed that the Fe_2 dimer was coordinated with six N atoms (Fe_2N_6) (Fig. 12a–c). Theoretical calculations showed that $CO_2 \rightarrow *CO_2$ is an exothermic process (−0.03 eV) at Fe_2N_6, while an energy barrier of +0.59 eV needs to be overcome at $Fe–N_4$. In addition, another CO_2 can be adsorbed at the Fe_2N_6 site to form a simultaneous adsorption of *CO and $*CO_2$, which is subsequently converted into a *CO and *CO configuration, and

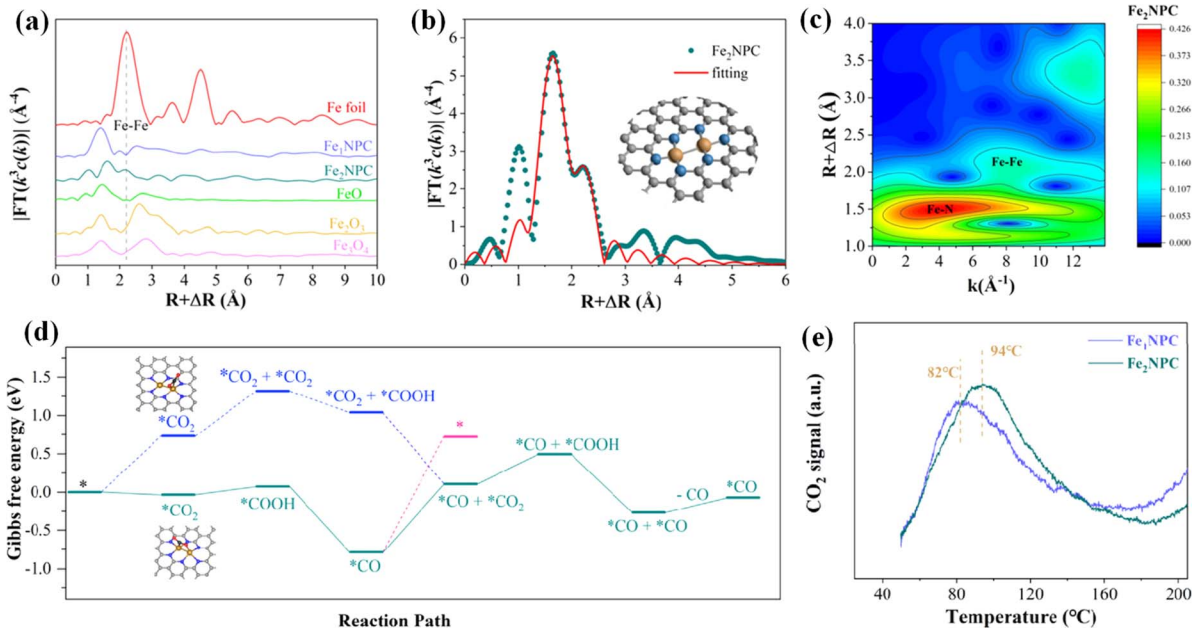

Fig. 12 (a) FT-EXAFS spectra at the Fe K-edge. (b) Corresponding EXAFS R-space fitting curves and (c) WT of Fe_2NPC. (d) Calculated free energy. (e) CO_2-TPD curves. Reproduced with permission.[125] Copyright 2022, American Chemical Society.

the desorption of CO requires only 0.20 eV. The maximum energy barrier of CO_2 to CO at the Fe_2N_6 site is 0.90 eV (Fig. 12d). The desorption temperature of CO_2 at the Fe_2N_6 site is also higher than that of Fe–N_4 (Fig. 12e). The synergistic effect of the Fe_2 dimer is conducive to the adsorption of CO_2 and the desorption of CO.

2.2.2.2. Heteronuclear DACs. The synergistic effect of bimetallic active sites can break the linear proportional relationship of single atomic sites, which is conducive to catalysing complex multi-electron reactions and improving the stability.[126] The electron coupling of adjacent metal sites can optimize the adsorption energy and adsorption mode of reaction intermediates, reduce the energy barrier and accelerate the reaction kinetics. Due to the unique electronic structure of DACs, great progress has been made in electrocatalytic reactions such as the HER, OER, ORR, CO_2RR and NRR.[9,127]

The development of high-performance DACs is expected to replace platinum for the HER. Fan *et al.* prepared a W_1Mo_1-NG DAC with W–O–Mo–O–C structure by combining a hydrothermal method and chemical vapor deposition (CVD) technology.[128] The W and Mo diatomic structure is the active center of the HER and has high stability. Theoretical calculations showed that the electron delocalization of the W–O–Mo–O–C configuration provided the best adsorption strength for H and accelerated the kinetics of the HER. Hu *et al.* used atomic layer deposition to anchor Pt to Ni and N co-doped carbon (PtNi-NC), exhibiting an η_{10} of 30 mV for the HER in an acidic medium.[129] XAS characterization indicated the presence of a Pt–Ni dimer in the PtNi-NC. DFT calculations showed that Pt–Ni is beneficial to regulate adsorption energy and increase catalytic activity by regulating the local electronic structure and charge. Liu *et al.* studied cobalt-based DACs (Co–M DACs) for the HER and found that the activity of DACs was significantly better than that of a single-atom Co catalyst.[130] Theoretical calculations showed that OH is more easily adsorbed on the CoFe DAC, promoting hydrogen evolution under alkaline conditions.

The ORR and OER are the core reactions of various energy conversion devices, and their main challenge is the complex four-electron transfer process with a high overpotential. Fu *et al.* used a plasma engineering method to immobilize an Fe–Co dimer onto mesoporous nitrogen-doped carbon nanotubes (Fe, Co SAs-PNCF) with metal loading of up to 9.8 wt%.[131] Fe, Co SAs-PNCF showed good ORR activity (E_{onset} = 1.04 V and $E_{1/2}$ = 0.93 V). XAS analysis revealed that the active center of the Fe, Co SAs-PNCF catalyst is the N_3–Fe–Co–N_3 structure. *In situ* XAS and Raman spectroscopy were used to study the changes of oxidation states of Fe and Co and the bond length of the N_3–Fe–Co–N_3 structure during the ORR. The Raman peak intensities of

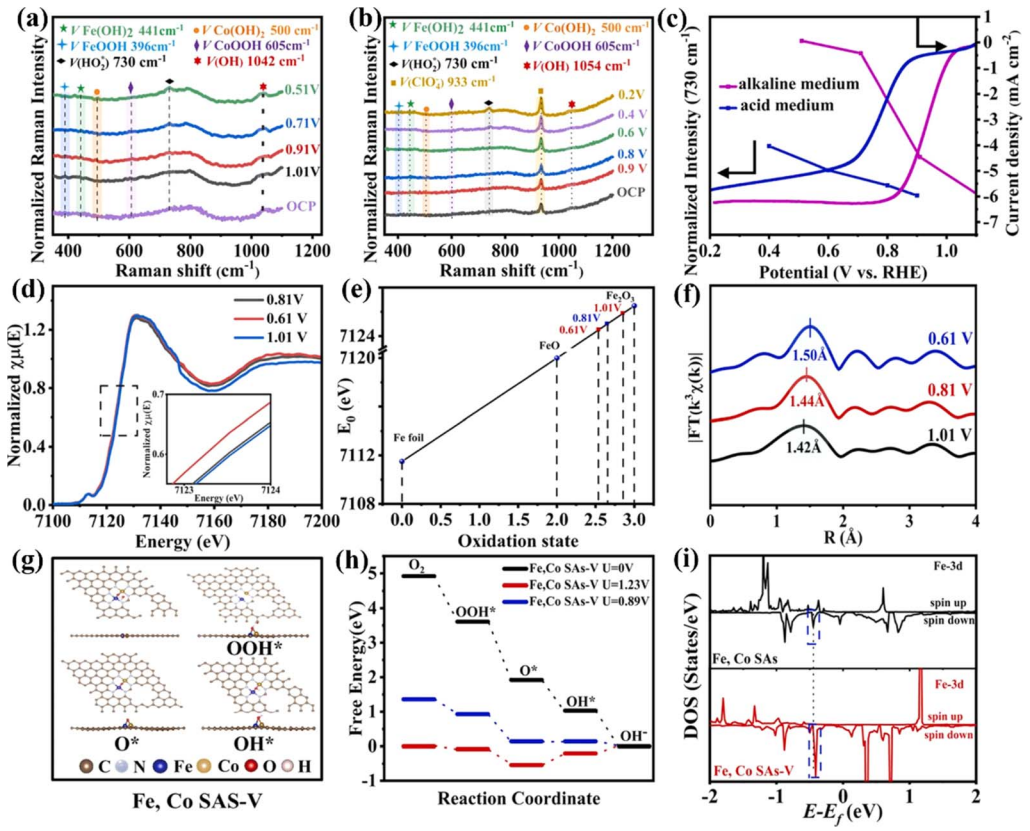

Fig. 13 Potential-dependent *in situ* Raman spectra during the ORR process in (a) alkaline and (b) acidic solutions. (c) Normalized Raman intensities of the stretching mode of OOH at 730 cm^{-1}. (d) *In situ* XAS spectra recorded at the Fe K-edge. (e) Fitted average oxidation states of Fe from XANES spectra. (f) Lengths of the Fe–N bond obtained from the FT-EXAFS spectra. (g) Optimized structures of OH*, O*, and OOH* intermediates on the Fe, Co SAs-PNCF surfaces. (h) Free energy diagram. (i) Electronic density of states (DOS). Reproduced with permission.[131] Copyright 2021, Elsevier Ltd.

CoOOH/FeOOH and $Fe(OH)_2/Co(OH)_2$ changed with increasing bias, and oxygen intermediates on the catalyst surface increased continuously, indicating that Fe/Co species are the active sites (Fig. 13a–c). *In situ* XAS results showed that the oxidation states of Fe and Co become smaller and Fe/Co–N bonds become longer during the ORR process at lower voltages (Fig. 13d–f), indicating that the N_3–Fe–Co–N_3 structure is the active center of the ORR. Theoretical calculations were further used to reveal the mechanism of the ORR. The limiting potential (U_L) of Fe, Co SAs–V (0.89 V) is higher than that of Fe, Co SAs (0.81 V) and NCF (0.278 V). The spin orbit of Fe, Co SAs-V is closer to the Fermi level, and the transfer of electrons between metal and oxygen atoms facilitates electron accumulation and accelerates the ORR process (Fig. 13g–i).

Hu *et al.* synthesized a cobalt–iron diatomic catalyst using *in situ* electrochemistry by introducing iron onto a single-atom Co catalyst.[132] The dimerized Co–Fe structure is the active site of the OER. Lou *et al.* synthesized a nitrogen-doped carbon material (a-NiCo/NC) anchored by Ni–Co sites using a multi-step template strategy, in which Ni and Co are dispersed on hollow prisms of the carbon.[133] DFT calculations showed that the strong interaction between Ni and Co sites optimizes the electronic structure, reduces the reaction energy barrier, and increases the OER activity. Wu *et al.* obtained a diatomic catalyst (FeCo-NC) by calcining an Fe and Co co-doped zeolite imidazole skeleton (ZIF-8).[134] FeCo-NC showed good bifunctional catalytic activity, exhibiting $E_{1/2}$ of 0.877 V in the ORR and $E_{j=10}$ of 1.579 V in the OER. The increase in the activity of the ORR and OER can be attributed to the adjustable electronic structure of FeCo–N_6. In addition, the fractional micropore–mesopore structure of the catalyst can increase the specific surface area and facilitate mass transfer.

Compared with SACs, DACs provide a variety of adsorption sites for the CO_2RR, and the synergistic effect between diatomic sites can improve the selectivity of CO_2 conversion to CO and regulate the electronic structure to promote the subsequent reaction. The CO selectivity on the diatomic Ni–Fe catalyst synthesized by Zhao *et al.* was as high as 98% at −0.7 V, and the electron interaction between Ni and Fe is beneficial to COOH* formation and CO desorption.[33] Wu *et al.* synthesized a diatomic catalyst with Co–Cu heterodiatomic pairs, which has an FE of 99.1% for CO generation and FE_{CO} of more than 95% at high current densities.[135] The introduction of the second metal can effectively regulate the electronic structure and promote the formation of intermediate *COOH. He *et al.* prepared a nitrogen-doped carbon matrix catalyst with Fe–Cu diatomic sites, and the CO FE in the CO_2RR was as high as 99.2%.[136] The synergistic effect of Fe–Cu accelerates the charge transfer, and effectively regulates the position of the d-band center, reducing the reaction energy barrier. He *et al.* prepared a Ni/Cu–N–C catalyst with Ni–Cu double sites, in which an N_4Ni/CuN_4 site structure was formed (Fig. 14a–c).[137] The catalyst had an FE_{CO} of 99.2% at −0.79 V. Theoretical calculation results showed that the adjustment of electronic structure promoted by the two-site interaction can effectively narrow the band gap, promote charge transfer, and reduce the reaction energy barrier, which is conducive to the generation of CO (Fig. 14d–f).

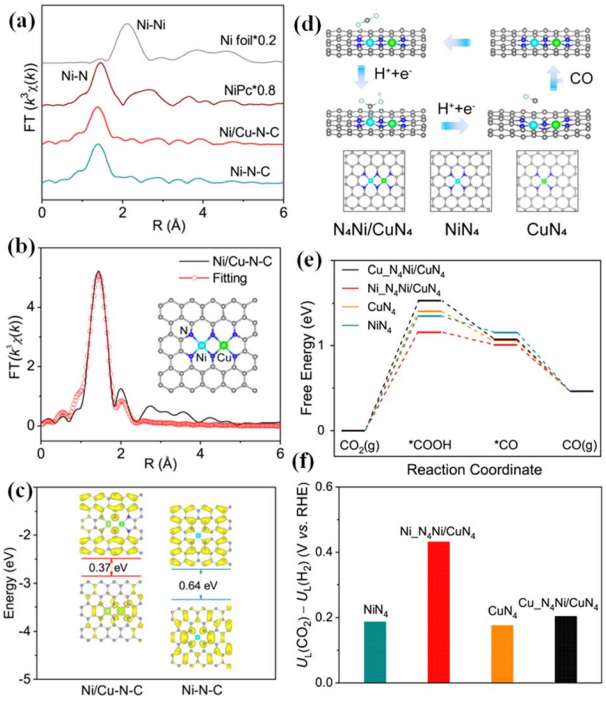

Fig. 14 (a) Ni K-edge FT-EXAFS curves. (b) Ni K-edge EXAFS fitting curves of Ni/Cu–N–C in the R space. (c) HOMO and LUMO spin electron densities of the proposed Ni/Cu–N–C and Ni–N–C models. (d) Optimized catalytic models and reaction pathways. (e) Free energy profiles of the CO_2RR. (f) Difference in limiting potentials for the CO_2RR and HER. Reproduced with permission.[137] Copyright 2021, American Chemical Society.

At present, C_1 products are mainly reported on DACs in the catalytic CO_2RR, and further in-depth products have been rarely reported. The mechanism of multi-electron reaction to produce methane and methanol on DACs for the CO_2RR was explored, demonstrating the way of C–C coupling to obtain C_2 products. Lu *et al.* constructed Fe/Co SACs and found that CO was the only product in the CO_2RR.[138] With the help of CO intermediates, the limiting potential on the FeCo-NC DAC to reduce CO_2 to CH_3OH and CH_4 is as low as −0.64 V. Under applied voltage, FeCo-NC is more likely to generate CH_3OH and CH_4, since the two-site center facilitates spin polarization and electron transfer. *CO tends to adsorb the bridge position of the dual-sites on either side, and C–C coupling is not easy to occur since greater excitation energy is required. In addition, the increase of CO concentration at the dual-sites will cause poisoning.[139]

2.2.3. Regulating the electronic structure of TACs. DACs are an important improvement over SACs, and on this basis, TACs can be fabricated by continuing to adjust the number of central metal atoms, providing more space for the regulation of electronic structure.[140] Compared with SACs and DACs, TACs with suitable coordination structure have the potential to catalyse complex reactions with multiple electron and proton coupling processes. However, due to the difficulty of controllable synthesis and the complexity of electronic structure, the research on TACs is still in the initial stage. The electronic structure can be adjusted by optimizing the metal configuration

of active sites. In addition, the structural symmetry of active sites also significantly affects electron distribution. Wu *et al.* designed a trinuclear catalyst with a manganese atom and two cobalt atoms coordinated with eight nitrogen atoms (Co_2MnN_8/C).[38] Co_2MnN_8/C can efficiently catalyse the ORR with a half-wave potential of 0.912 V. DFT calculations showed that Co_2MnN_8–2OH formed by the combination of Co_2MnN_8 and OH was the active site of the ORR, which led to the rearrangement of d electrons and optimized the adsorption energy of the reaction intermediates. Li *et al.* prepared atomically dispersed Ru_3 on a nitrogen-doped porous carbon catalyst by cage separation and pyrolysis.[31] The cage of ZIF-8 can just wrap $Ru_3(CO)_{12}$ molecules, and uniform nitrogen-fixed Ru_3 clusters were synthesized by annealing (Fig. 15). HAADF-STEM and XAS results showed that Ru_3 clusters have a triangular structure, and Ru–N coordination and Ru–Ru metallic bonds were detected, indicating that the nitrogen coordination effectively stabilized Ru_3 clusters. Liu *et al.* prepared a trinuclear copper-based cluster (Inz-Cu_3) catalyst to research the effect of structural symmetry on the selectivity of CO_2RR products by changing the distance and angle between adjacent Cu active sites.[141] The experimental results showed that at the current density of −320 mA cm^{-2}, the Faraday efficiency of CO_2 conversion to C_2 is 42.20% under acidic conditions, and under alkaline conditions, the Faraday efficiency of CO_2 conversion to C_2 is 66.79%, with $FE_{C_2H_4} = 35.27\%$ and $FE_{C_2H_5OH} = 31.52\%$. Liao *et al.* synthesized a stable and inexpensive metal-azo salt trinuclear copper cluster catalyst (Cutrz) that efficiently catalysed CO_2 to ethylene and C_{2+} with Faraday efficiencies of up to 50% and 80%, respectively.[142] Theoretical calculations showed that three CO intermediates can be closely adsorbed on the same side of Cu clusters, accelerating the C–C coupling probability. Yagi *et al.* used graphene oxide and polynuclear copper precursors to synthesize an electrocatalyst with trinuclear copper sites through a rapid heating strategy, which can effectively catalyse the ORR at pH = 7, exhibiting an initial potential of 0.82 V and good stability.[143]

To study the synergistic effect between three nuclear metal atoms, Wang *et al.* systematically simulated the catalytic performance of single atoms, dual atoms and triple atoms in the electrocatalytic NRR by theoretical calculations.[144] The

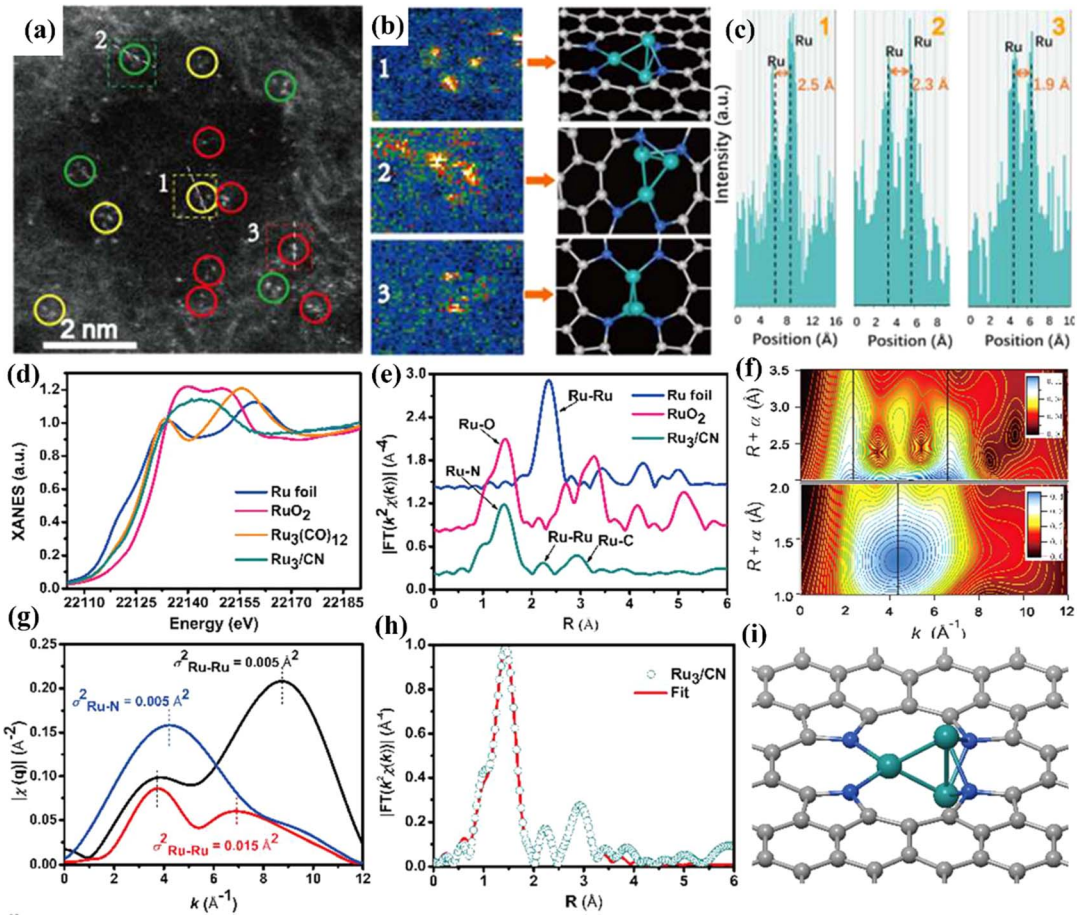

Fig. 15 (a) HAADF-STEM image of Ru_3/CN. (b) Corresponding intensity maps (left), models (right) and (c) intensity profiles obtained in areas labeled 1, 2, and 3 in (a). (d) Ru K-edge XANES spectra. (e) EXAFS Fourier transformed (FT) k^2-weighted $\chi(k)$ function spectra. (f) Wavelet transforms for the k^2-weighted Ru K-edge EXAFS signals for the high-coordination shells in Ru_3/CN. The colors in the contour figures indicate the moduli of the Morlet wavelet transform. (g) Comparison of the q-space magnitudes for FEFF-calculated k^2-weighted EXAFS paths. (h) Corresponding EXAFS R-space fitting curve for Ru_3/CN. (i) Schematic model of Ru_3/CN. Reproduced with permission.[31] Copyright 2017, American Chemical Society.

results showed that the catalytic activity of the TAC was generally superior to that of the SAC and DAC since the reduction of adsorption energy of the NH_2 intermediate effectively promotes the rate control step of $*NH_2$ hydrogenation. Due to the relatively low loading capacity of single/double/triple site catalysts, there are few active sites which affect the catalytic activity. Jiang *et al.* used density functional theory to construct a triatomic Fe_3-GDY/Gra catalyst with a theoretical mass loading of up to 35.8 wt%, showing excellent activity in the theoretical NRR at a potential of −0.37 V.[145] High loading provides more active sites to activate N_2 more easily. Zhou *et al.* theoretically demonstrated that a trinuclear catalyst anchored on nitrogen-doped carbon can effectively convert CO_2 into C_2 and C_{2+} products in the CO_2RR.[21] The trinuclear active sites can adsorb multiple CO_2 at the same time, which is conducive to C–C coupling.

2.3. Regulating the coordination environment of central metal sites

Electrocatalytic active sites are formed by bonding between central metal atoms and the surrounding coordination atoms. Therefore, adjusting the bonding mode can tune the electronic structure of central metal atoms, including the valence and spin states and the electron cloud density near the Fermi level. The target active structure is obtained by adjusting the number, type and configuration of coordination atoms, which is conducive to understanding the relationship between coordination configuration and catalytic performance.[146,147]

2.3.1. Adjusting the number of coordination atoms. $M–N_x$ coordination structures have attracted much attention due to their high electrocatalytic activity and durability. For SACs, isolated single metals have high surface free energy, and easily migrate and reunite. This process can be effectively prevented through the interaction between metal and N atoms.[148–150] The usual ways to synthesize $M–N_x$ coordination structures are directly annealing metal- and nitrogen-containing precursors in an inert nitrogen atmosphere. By regulating the number of N atoms in the $M–N_x$ ($x = 1$–5) coordination structure, the electronic structure of the active site can be effectively regulated, thus promoting the catalytic effect on the HER, OER, ORR, CO_2RR and NRR.[39,114,151]

Among them, the $M–N_4$ structure is the most studied active site, which is like that of metal porphyrins and metal phthalocyanines, but the chemical environment after loading on the carbon carrier is obviously different from that of metal porphyrins/metal phthalocyanines. $M–N_4$ sites showed good activity for many electrocatalytic reactions. Guo *et al.* synthesized single-atom Co and Ni catalysts through three steps of impregnation–carbonation–acidification.[152] The single-atom Co catalyst showed excellent catalytic activity and stability for the OER/ORR, and the reversible oxygen overpotential was 0.75 V. It was assembled as a cathode into a zinc–air battery with a capacity of 530.17 mA h g_{zn}^{-1}. Theoretical calculation results showed that the OH* hydrogenation barrier increases when there are clusters in the catalyst, which is not conducive to the promotion of ORR/OER activity.

Xie *et al.* synthesized a $Ni–N_4–C$ catalyst using a top-ochemical transformation strategy, which effectively avoided the agglomeration of Ni metal.[153] The FE of converting CO_2 to CO was up to 99%. Theoretical calculations showed that the $Ni–N_4$ site effectively reduces the generation energy of COOH* and accelerates charge transfer to promote the conversion of CO_2 to CO (Fig. 16a–e). The distance between different $M–N_x$ coordination structures affects the selectivity of the CO_2RR. Zheng *et al.* adjusted the $Cu–N_x$ structure by adjusting pyrolysis temperature and Cu doping amount.[154] Experimental and theoretical results showed that $Cu–N_x$ can promote the conversion of CO_2 to CH_4 when the concentration of Cu is less than $2.4\%_{mol}$, while when the concentration is increased to $4.9\%_{mol}$, CO_2 can be transformed into C_2H_4. Two CO intermediates can be coupled to produce C_2H_4 at adjacent $Cu–N_2$ sites (Fig. 16f).

Fu *et al.* used *in situ* XAS to reveal the relationship between the ORR and the configuration of active sites.[155] They studied the dynamic changes of the $Mn–N_4$ configuration during the ORR process. Under applied voltage, $Mn–N_4$ was transformed into $Mn–N_3C$, and then further transformed into the $Mn–N_2C_2$ configuration. The valence state of Mn increased from +3.0 to +3.8 and then decreased to +3.2. Therefore, $Mn–N_3C$ and $Mn–N_2C_2$ configurations really regulated the adsorption energy barrier and adsorption mode of the reaction intermediates in the ORR process. Wang *et al.* synthesized nitrogen-doped graphene with highly dispersed FeN_5 active sites, which achieved 97.0% FE in converting CO_2 to CO.[156] Theoretical calculations showed that five N coordination depleted the electron density of Fe 3d, effectively promoting the formation of CO. Jiang *et al.* prepared single-atom $Ni–N_x–C$ with different N coordination numbers by a post-synthetic metal substitution method.[157] The FE on the $Ni–N_3–C$ catalyst was 95.6%, which is significantly higher than that of the $Ni–N_4–C$ catalyst. DFT calculations showed that the $Ni–N_3$ site was conducive to COOH* production and accelerated CO production. Wang *et al.* reasonably designed a single-atom W catalyst with a $W_1N_1C_3$ structure, showing an η_{10} of 85 mV in 0.1 M KOH solution for the HER.[62]

In DACs, the M_1M_2-N_6 coordination structure is usually formed. Zhao *et al.* anchored diatomic Ni–Fe sites on carbon nitride, which showed an FE_{CO} of up to 90% and CO_2RR stability.[158] Theoretical calculations revealed that the $NiN_3–FeN_3$ active site reduced the formation energy of the COOH* intermediate and the desorption energy of CO. In addition, other $M_1M_2–N_x$ coordination structures also play an important role in the CO_2RR. Lu *et al.* anchored diatomic $Ni_2–N_3$ sites onto carbon nanotubes (CNTs), on which the energy barrier of the *COOH intermediate could be more significantly reduced than on $Ni–N_3$, $Ni–N_4$ and $Ni_2–N_4$ sites.[159] The energy barrier of the rate-limiting step of *CO desorption is 0.76 eV, which is conducive to the conversion of CO_2 to CO. Zhong *et al.* reported three coordination modes of $Ni_2–N_7$, $Ni_2–N_5C_2$ and $Ni_2–N_3C_4$, among which $Ni_2–N_3C_4$ showed excellent activity in the CO_2RR.[160] DFT calculations showed that a suitable coordination environment regulated the electronic structure of Ni_2 and reduced the energy barrier of COOH*.

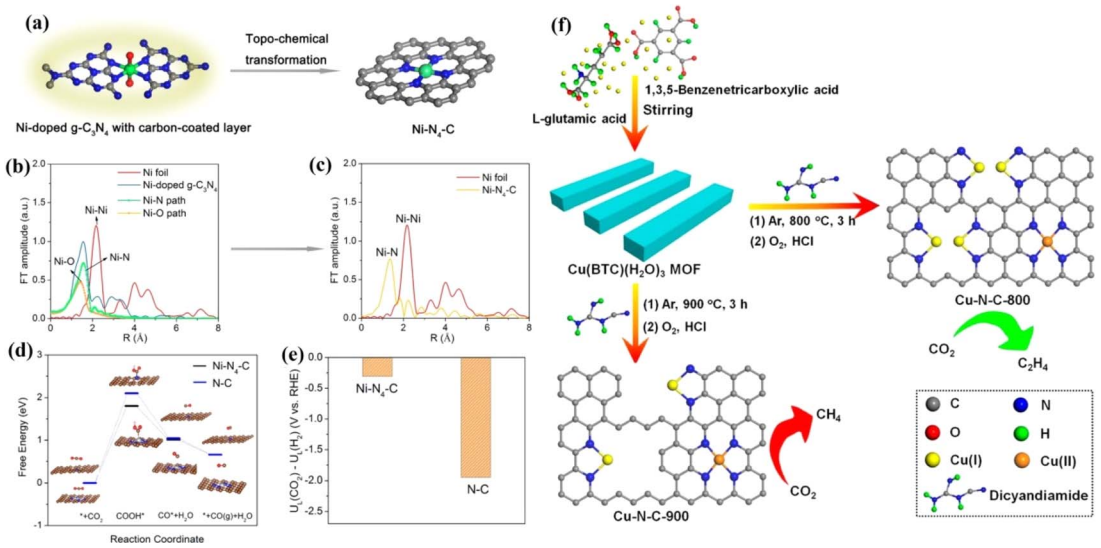

Fig. 16 (a) Schematic illustration of the topochemical transformation strategy. (b) FT of the Ni K-edge EXAFS oscillations of Ni-doped g-C_3N_4. (c) FT of the Ni K-edge EXAFS oscillations of Ni–N_4–C. (d) Calculated free energy diagram. (e) Difference in limiting potentials for CO_2 reduction and H_2 evolution. (f) Schematic of the procedure to synthesize Cu–N–C–T catalysts. (a–e) Reproduced with permission.[153] Copyright 2017, American Chemical Society. (f) Reproduced with permission.[154] Copyright 2020, American Chemical Society.

The Fe–N_x structure has been considered to be an effective active site for the ORR.[161–163] However, a two-electron transfer process will inevitably occur, generating a small amount of H_2O_2, which attacks N ligands, resulting in the dissolution of Fe and inactivation. To inhibit the two-electron ORR process, it is needed to regulate the Gibbs free energy of *OOH to prevent the spontaneous generation of H_2O_2.[164,165] By introducing a second metal, the electronic structure of Fe–N_4 can be effectively adjusted to optimize the adsorption free energy of reaction intermediates.[166] Cao *et al.* synthesized a diatomic catalyst (Fe–Mn–N–C) with FeN_4–MnN_3 sites.[167] There is a defect around FeN_4–MnN_3 and the Fe–Mn bond has a strain effect, leading to a significant change of the space charge density around Fe and Mn. The rate-limiting step of the ORR on FeN_4 is OH* → H_2O, while it changes to O* → OH* after the introduction of MnN_3. The intermediate OOH* is adsorbed at the Fe–Mn bridging position, which is conducive to O–O dissociation, and hydrogen peroxide generation by $2e^-$ can be completely inhibited. The FeN_4–MnN_3 configuration decreased the d-band center of FeN_4 compared with FeN_4, and weakened the binding strength, thus reducing the adsorption energy of oxygen-containing intermediates (Fig. 17).

2.3.2. Regulating the type of coordination atoms. In addition to the N ligand, S, P, B, O and other nonmetallic elements can also be used to regulate the local electronic structure of metal active sites. S has a good affinity for transition metal elements, and can coordinate with the central metal atom to form the M–N_xS_x structure, so that the local charge of the active center is rearranged. Zhu *et al.* designed an S and N co-doped single-atom Fe catalyst with excellent OER/ORR bifunctional activity.[168] S doping modulates the charge and spin distribution around Fe–N_x and improves the catalytic activity. Li *et al.* synthesized an N and S co-coordinated Cu single-atom (S-Cu-ISA/SNC) with a hierarchically porous structure.[169] XAS results showed Cu–N (1.55 Å) and Cu–S (1.81 Å), and the FT-EXAFS indicated that the central metal Cu coordinated with three N

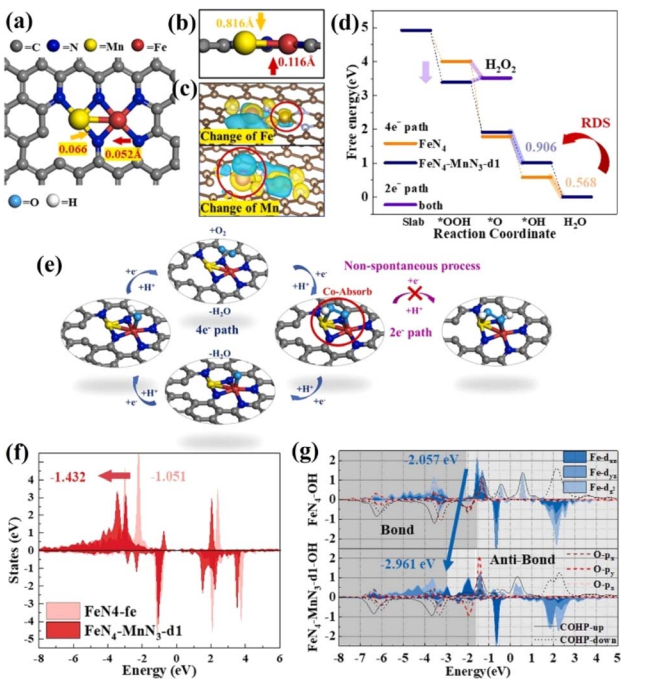

Fig. 17 (a) FeN_4–MnN_3-d1 structure (d1 referring to the number of defect being 1). (b) Side view of the FeN_4–MnN_3 structure. (c) Charge density difference diagrams of FeN_4–MnN_3-d1. (d) Oxygen-free energy diagrams of FeN_4 and FeN_4–MnN_3-d1. (e) Illustrations of the ORR process on the FeN_4–MnN_3-d1 structure. (f) The d-band changes of Fe in FeN_4 and FeN_4–MnN_3-d1. (g) PDOS of Fe in the d_{xz}, d_{yz} and d_{z^2} orbitals and the bonding and anti-bonding state information obtained by COHP. Reproduced with permission.[167] Copyright 2020, Elsevier B.V.

and one S (Fig. 18a). The S-Cu-ISA/SNC catalyst with an asymmetric Cu–S_1N_3 structure can efficiently catalyse the ORR with a half-wave potential of 0.918 V. Subsequently, to study the change of Cu structure in the ORR, *in situ* XAS tests were conducted. The valence of Cu changed from +2 to +1, and the length of the Cu–N bond was shortened from 1.98 Å to 1.94 Å (0.90 V) and 1.93 Å (0.75 V), while the length of the Cu–S bond was almost unchanged (Fig. 18b–g). According to the volcano-type plot (Fig. 18h), Cu–N_4 and Cu–S_1N_3 are located at the right side, indicating that during the ORR process, the intermediate adsorption at the Cu sites is weak (Fig. 18i).

P and N belong to the same group V, but the electronegativity of P is weaker than that of N, and therefore, the adsorption activity of reaction intermediates can be regulated by introducing P in the common tetragonal configuration. Wang *et al.* synthesized a single-atom Co catalyst (Co-SA/P-*in situ*) with a Co_1–P_1N_3 coordination structure, showing an η_{10} of 98 mV for the HER.[170] The bond lengths of Co–P and Co–N were 2.18 Å and 1.95 Å, respectively. *In situ* XAS results showed that the valence state of Co increased from +1.53 to +1.78 during the HER, and the bond lengths of Co–P and Co–N became longer, indicating that Co_1–P_1N_3 was the active center. DFT calculations showed that P and N doping promoted the charge transfer, and effectively improved the catalytic activity of the HER. Chen *et al.* found that a N- and P-codoped single-atom Fe catalyst (Fe–N/P–C) can efficiently catalyze the CO_2RR, and the FE_{CO} can reach 98%.[171] DFT calculations showed that the introduction of P reduces the oxidation state of Fe, optimizes the adsorption energy of the *CO intermediate, and improves the catalytic activity.

B is an electron-deficient atom, and when B and N co-coordinate with the metal, B shares electrons with the electron-rich N to regulate the electronic structure around the metal. Xin *et al.* synthesized a single-atom Ni catalyst (Ni–B/N–C) with a Ni–B_1N_3 coordination structure, exhibiting a half-wave potential of 0.87 V for the ORR.[174] Theoretical calculation results show that the introduction of B can adjust the local coordination environment of Ni–B_1N_3, reduce the adsorption energy

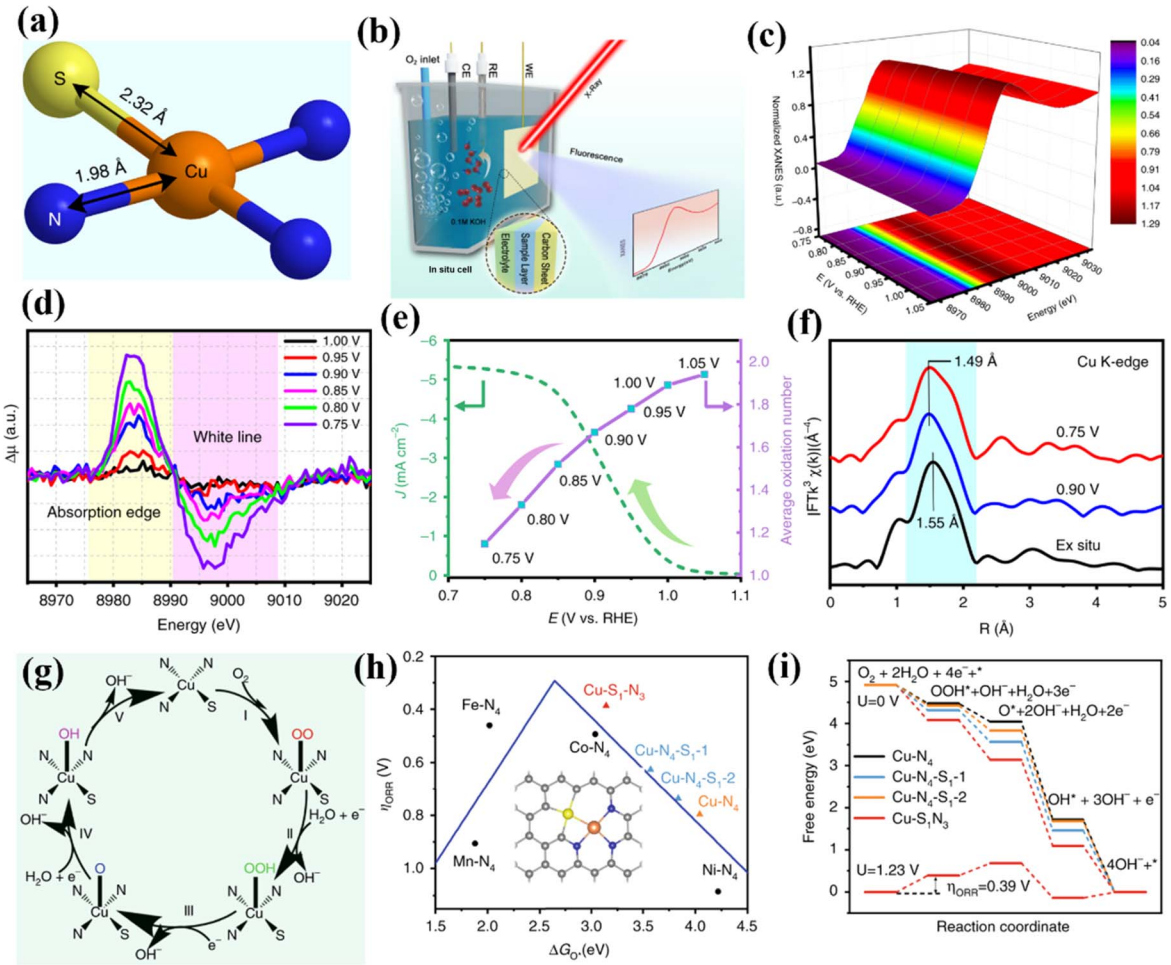

Fig. 18 (a) Schematic atomic interface model of S-Cu-ISA/SNC. (b) Schematic of the *in situ* electrochemical cell set-up. (c) Cu K-edge XANES spectra of S-Cu-ISA/SNC at various potentials during the ORR. (d) Differential $\Delta\mu$ XANES spectra. (e) Current density as a function of potential for S-Cu-ISA/SNC (left) and the average oxidation number of Cu species in S-Cu-ISA/SNC as a function of potential (right). (f) k^3-weighted FT-EXAFS. (g) The proposed ORR mechanism for the S-Cu-ISA/SNC. (h) η_{ORR} as a function of ΔG_{O*} on different Cu-centered moieties. (i) Free-energy diagram. Reproduced with permission.[169] Copyright 2020, Nature.

barrier of reaction intermediates, and accelerate the ORR process.

The electronegativity of O is greater than that of N, and O and N can form quad-coordination with the metal in the plane and quintuple coordination outside the plane. Compared to other non-metallic coordination atoms, no additional oxygen source is introduced during the synthesis process due to the presence of oxygen in most carbon precursors. Chen *et al.* successfully introduced single-atom Mn–N_3O_1 into a 3D graphene framework (Mn/C–NO), optimized the position of the Mn d-band center by regulating the geometry of local coordination, making it conducive to the adsorption and desorption of reaction intermediates, and accelerating the kinetics of the ORR.[175] Chen *et al.* used a sacrificial template method to controllably anchor Ni–N_4–O sites on nitrogen-doped porous graphite carbon (NiSA-N-PGC).[172] The highest FE of NiSA-N-PGC in the catalytic conversion of CO_2 to CO was 97.2%. *In situ* infrared spectroscopy was used to study the reaction intermediates adsorbed on the catalyst surface, demonstrating that *COOH and *CO were the main intermediates in the CO_2RR process. With the increase of potential, the peak strength of *CO increased, while the peak strength of *COOH decreased,

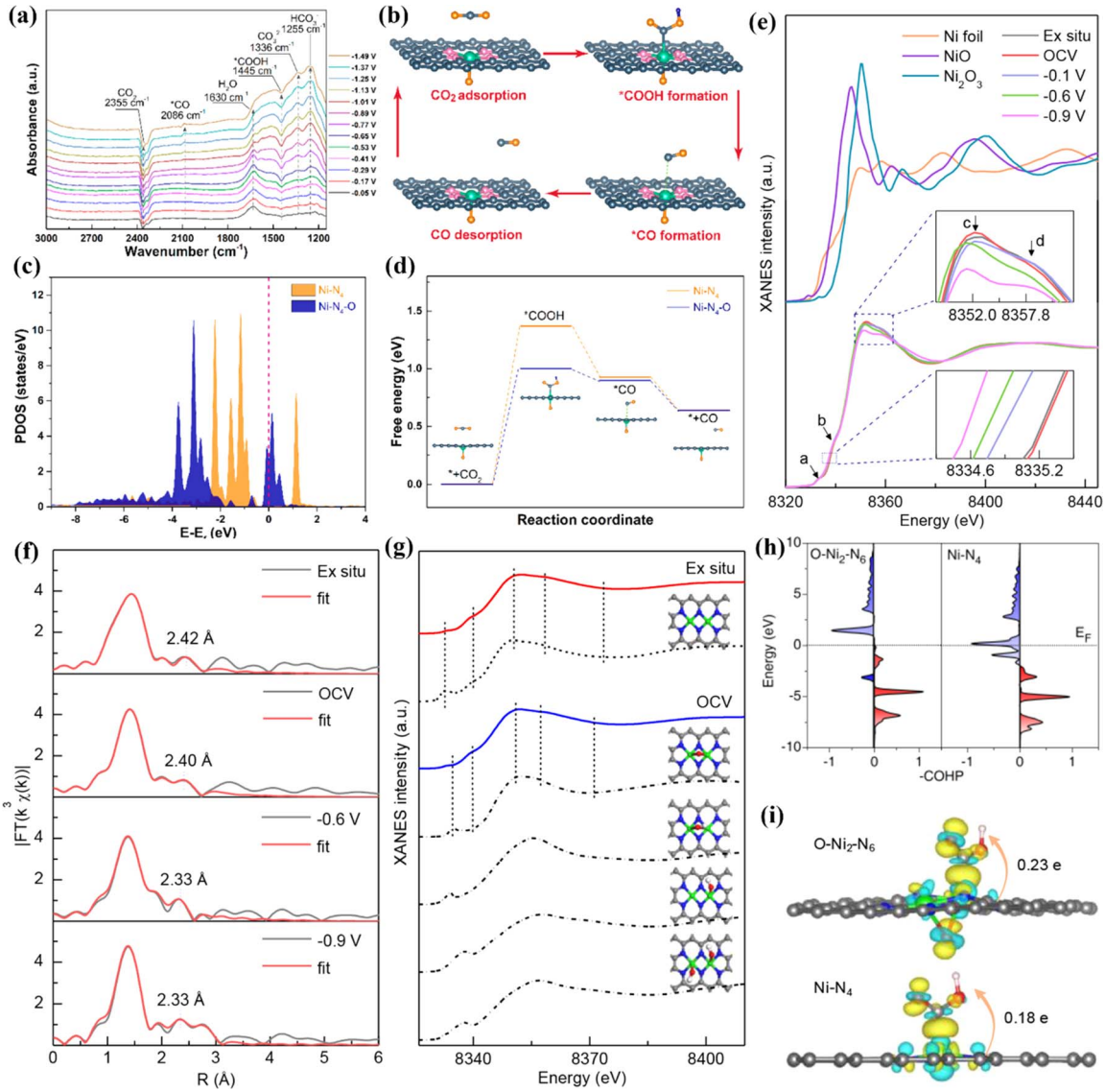

Fig. 19 (a) Potential-dependent operando attenuated total reflection surface enhanced infrared absorption spectroscopy (ATR-SEIRAS) spectra of NiSA(0.3)-N-PGC. (b) Proposed reaction steps of electrocatalytic reduction of CO_2 to CO over the Ni–N_4–O site. (c) PDOS calculated using DFT for Ni 3d. (d) Reaction paths and free energy diagrams. (e) Operando XANES spectra recorded at the Ni K-edge of Ni DSC. (f) Least-squares curve-fitting analysis of operando EXAFS spectra at the Ni K-edge. (g) Comparison between the Ni K-edge XANES experimental spectra (solid lines) and the theoretical spectra. (h) Projected crystal orbital Hamilton population (pCOHP) between the metal center and the COOH* intermediate. (i) Electron density difference plot of the *COOH intermediate adsorption structure and the Bader charge analysis. (a–d) Reproduced with permission.[172] Copyright 2022, American Chemical Society. (e–i) Reproduced with permission.[176] Copyright 2021, American Chemical Society.

indicating that *COOH → *CO accelerated, and the activity of the CO_2RR increased. Theoretical calculations revealed the promotion effect of the axial Ni–O coordination on the CO_2RR. In the CO_2RR, the conversion step of CO_2 to CO is CO_2 → *COOH → *CO → CO. The oxidation state of Ni in Ni–N_4–O is +1.12 e, which is higher than that in Ni–N_4 due to the transfer of electrons from Ni to the axial O. Therefore, the Ni 3d orbitals in the former exhibit higher DOS near the Fermi level than the latter. The coordination of axial O with high electronegativity enhances the electron delocalization of the active center metal Ni, reduces the reaction energy barrier in the CO_2RR, and facilitates the adsorption and desorption of reaction intermediates (Fig. 19a–d).

In DACs, the electron effect between two adjacent metal atoms can provide a variety of absorbable sites and accelerate electrocatalytic reactions. Hou *et al.* synthesized an atomically dispersed indium–nickel diatomic catalyst (InNi DS/NC), in which an oxygen atom is axially bridged between In and Ni.[173] XAS characterization showed that the coordination configuration was O–In–N_6–Ni, and the FE of CO generation was up to 96.7%. *In situ* characterizations and theoretical calculations showed that the interaction between the In–N_6–Ni site and bridging oxygen reduced the energy barrier of the *COOH intermediate and inhibited the competitive HER. In addition, the electrolyte can provide an oxygen atom axially between the two core metals and affect the activity and efficiency of the catalyst. Yao *et al.* synthesized a binuclear Ni cluster precursor and then anchored it to a nitrogen-doped carbon material to obtain Ni_2/NC with binuclear Ni_2–N_6 sites.[176] The FE of catalytic conversion of CO_2 to CO was greater than 94%. Operando XAS analysis and theoretical calculation results showed that the Ni_2–N_6 in the electrolyte first adsorbed an oxygen-containing group to form an O–Ni_2–N_6 structure during the initial reaction, and then the CO_2 adsorbed on the O–Ni_2–N_6 structure was rapidly activated, and then the CO* intermediate was obtained through two proton coupling processes. Finally, CO* was desorbed on the O–Ni_2–N_6 structure. The occupancy rate of Ni–COOH* antibonding states at O–Ni_2–N_6 is lower than that at Ni–N_4, indicating stronger adsorption of intermediates at the former. In addition, the positive charge (0.23 e) at O–Ni_2–N_6 was higher than that at Ni–N_4 (0.18 e), indicating that the O–Ni_2–N_6 site was more conducive to the activation of CO_2 conversion to COOH* (Fig. 19e–i).

3. Theoretical understanding of atomic catalysts for electrocatalysis

Electrocatalytic reactions usually take place at the interface or surface of catalysts, and structural variations affect the adsorption and the desorption. On the one hand, well-designed engineering of the geometry or electronic structure produces synergistic effects that can enhance catalytic activity, stability and selectivity. On the other hand, the changes in the electronic structure affect the charge density and the degree of d-band filling in the spin state, which modulates the binding model, leading to a decrease in the reaction energy and an increase in the catalytic activity.[68,177,178]

3.1. Synergistic effect

Modulating the coordination environment and electron distribution of atomic catalysts is an effective but still challenging strategy to improve the electrocatalytic performance.[179] Many works have shown the activity of DACs and TACs is higher than that of SACs due to a synergistic effect.[68] The synergistic effect between polynuclear metal atoms can regulate the local electronic structure, promote the transfer of electrons, optimize the adsorption and desorption properties, and reduce the overall reaction barrier, thus improving the electrocatalytic performance.[41] Theoretical calculations showed that the synergistic action of neighboring metals optimizes the d-band center positions of the metal centers and balances the free energies of the oxygen intermediates, thus increasing the oxygen electrocatalytic activity. Bu *et al.* reported a homogeneously conceived FeCo-DACs/NC catalyst, in which the synergistic interaction between Fe and Co exerted a significant effect on the reaction barrier.[180] The tiny band gap of FeCo-DACs/NC increased the electronic conductivity and accelerated the electron transport. Meanwhile, the synergistic interaction between Fe and Co made the metal d-band center of FeCo-DACs/NC lower than the Fermi energy level and the energy level position closer to the 2p orbital of O than that of the corresponding SACs (Fig. 20a and b). Lee *et al.* reported a more efficient Fe_2–N–C electrocatalyst than Fe_1–N–C. The diatomic Fe orbital coupling led to the reduction of orbital energy levels and electron delocalization, which facilitated *CO desorption. The orbital coupling between the dual-site Fe atoms reduced the energy gap between the antibonding and bonding states in *CO adsorption (Fig. 20c–e).[181] Li *et al.* reported the construction of a bimetallic catalyst by introducing single-atom Co into the second ligand shell layer of the Fe center.[182] The addition of the Co atom to the d-band center in FeCo-NC (−0.98 eV) brought it closer to the Fermi energy level than Fe-NC (−1.61 eV), indicating that fewer electrons populate the antibonding orbitals of the active center, thus enhancing the phase hundred interaction between the active and adsorbed substances, and facilitating the subsequent substrate reaction (Fig. 20f).

3.2. Defect coupled spin state change

Defects are prevalent in heterogeneous materials, and can be used as active sites to fabricate specific catalysts or to promote catalytic performance. Defect engineering is an effective way to modulate the surface physical/chemical properties of catalytic materials, and the presence of defects will significantly change the electronic structure and chemical properties, leading to the formation of new physicochemical properties or strong synergistic effects, and thus optimizing the catalytic performance.[183] The change of defect-coupled spin states has gradually attracted more and more attention. Yang *et al.* reported that the charge redistribution of the attached exfoliated monolayer of iron phthalocyanine (FePc) could be effectively regulated using a defective graphene substrate with 585 defects.[184] The transfer of electrons from the 585 defects to FePc formed an electron-rich region on the Fe atoms, and the high-density electrons further elevated the d-band center of the Fe atoms. Obviously,

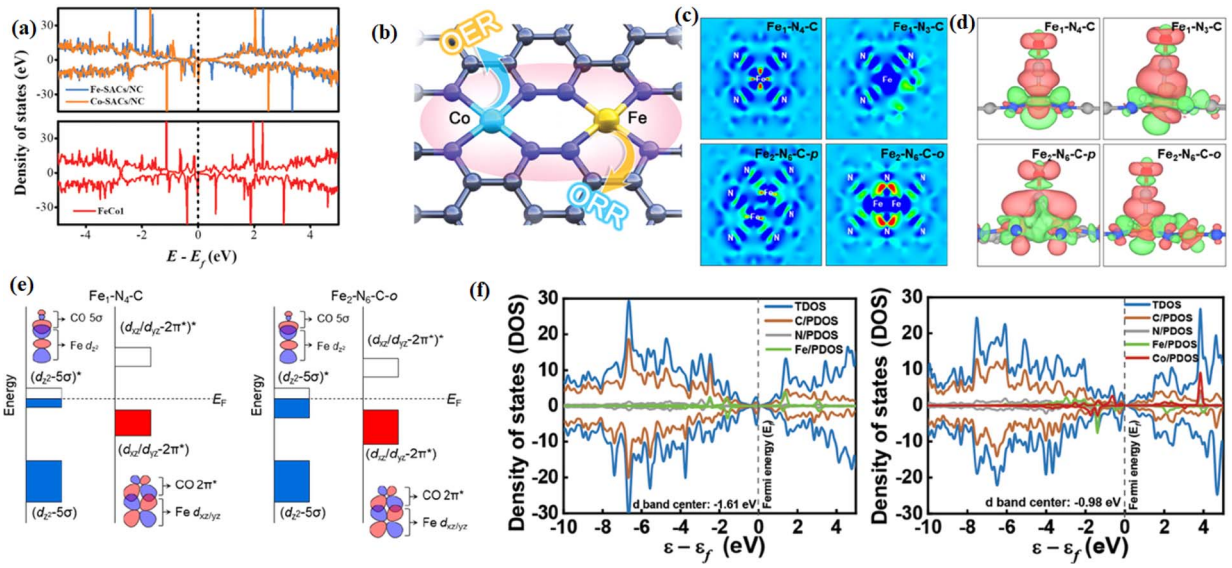

Fig. 20 (a) Proposed architecture of the Fe–Co metal pair in FeCo-DACs/NC. (b) DOS patterns of $FeCo_1$, Co-SACs/NC, and Fe-SACs/NC. (c) Bare surface with a range from $-0.01e$ Å^{-3}(blue) to $+0.04e$ Å^{-3} (red) and (d) *CO adsorption with an isosurface level of $0.002e$ Å^{-3}. (e) PDOS of Fe–N_4 and N_3–Fe–N–Co. (f) Schematic illustration of orbital interaction between Fe-3d (d_{z^2} and d_{xz}/d_{yz}) and adsorbed CO (5σ and 2π*) for Fe_1–N_4–C and Fe_2–N_6–C-o. (a and b) Reproduced with permission.[180] Copyright 2022, Wiley-VCH GmbH. (c and e) Reproduced with permission.[181] Copyright 2022, American Chemical Society. (f) Reproduced with permission.[182] Copyright 2023, Wiley-VCH GmbH.

this adjustment of the electronic structure of Fe atoms favoured the adsorption and reaction of O_2 molecules (Fig. 21a–c). Nitrogen-doped carbon-coupled $FeNi_3$ intermetallic compounds ($FeNi_3$@NC) with excellent OER and ORR properties were reported by Mu *et al.*[185] The defects in $FeNi_3$@NC, including impurities, dopants, vacancies, and interstitial defects, can significantly change the chemical properties and electronic structure, promoting the formation of new physicochemical properties or strong synergistic effects. Mai *et al.* utilized the coupling effect of edge defects of coordinated bismuth (Bi) and sulfur to improve the selectivity of the CO_2RR and inhibit the competing HER.[186] DFT calculations showed that sulfur tends to bind to the Bi edge defects, reduces the ligand-unsaturated Bi sites (*H adsorption sites), and modulates the charge state of the neighboring Bi sites to improve the *OCHO adsorption (Fig. 21d and e). Wang *et al.* utilized a seeded decarboxylate-induced defect strategy to improve the intrinsic activity of the Co SAC by increasing the defect density.[43] DFT calculations confirmed that in the defect-rich Co SAC, the defect structure formed near the Co–N_4 site likely influences the charge redistribution, which can greatly improve the intrinsic catalytic performance and reduce the free energy of OH adsorption on the Co–N_4 site, thus facilitating the electrochemical reaction.

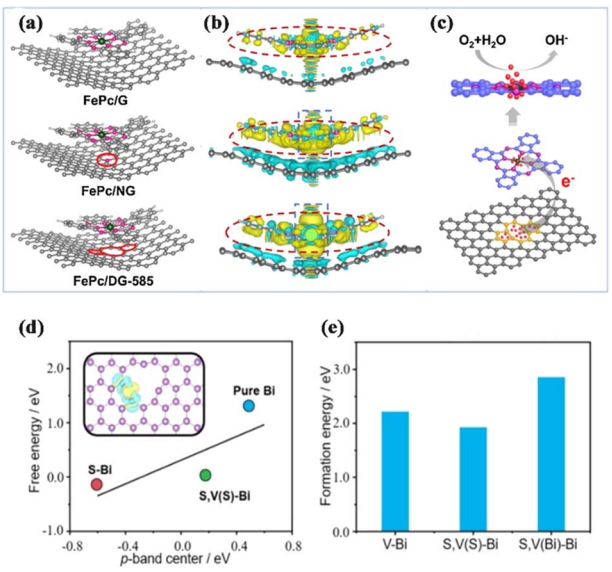

Fig. 21 (a) The top views of optimized FePc/DG-585 (FePc/G or FePc/NG) based hybrid interfaces. (b) The side views of the 3D charge density difference plot for the interfaces between the DG-585 (G or NG) sheet and FePc layer. (c) The schematic of a probable ORR electrocatalytic mechanism of FePc/DG-585 for the ORR. (d) The correlation between the adsorption energy (ΔG_{*OCHO}) and p-band center of active Bi atoms. (e) The formation energies. (a–c) Reproduced with permission.[184] Copyright 2020, Elsevier B.V. (d and e) Reproduced with permission.[186] Copyright 2023, Wiley-VCH GmbH.

3.3. Crystal field distortion spin state change

Although some previous discussions have demonstrated the important role of the coordination field of M–N–C catalysts in improving the catalytic performance, the mechanism is still unclear. Breaking the D_{4h} symmetry of the FeN_4 active center provides a new way to improve the activity of Fe–N–C catalysts.[187] Zhang *et al.* achieved the modulation of the electronic spin state of the Fe active center in SAC-Fe–N–C and the modulation of the electronic spin state of the FeN_4 active center from the low-spin state of FeN_5 to the high-spin states of FeN_4

and FeN_3, based on ligand-field theory by converting the defect-rich pyrrole-type N-coordinated FeN_x sites, thus allowing the electrons to easily penetrate the antibonding π-orbitals of oxygen.[188] Fe–N_4–HS has a three-dimensional electronic structure of t_{2g} and e_g, which promotes the kinetics of the ORR significantly. The asymmetric arrangement of the d-orbital electrons of Fe in the spin channel indicates spin polarization. Utilizing the activity-enhancing effect of the high spin state of Fe(III), the designed Fe–N_4-HS catalyst exhibited higher ORR activity than commercial Pt/C catalysts (Fig. 22a). Ling *et al.* showed the first crystal-field deformation of the FeN_4 portion achieved by the introduction of sulfur–oxygen-polar functional groups into Fe–N–C catalysts, and revealed that the disruption of FeN_4's D_{4h} symmetry leads to the rearrangement of Fe 3d electrons and increases the spin moment of the Fe center.[187] The effective spin-state manipulation optimized the adsorption energy of ORR intermediates, which significantly improved the intrinsic ORR activity of the Fe–N–C catalysts (Fig. 22b–d). Ruan *et al.* remodelled the metal-centered coordination of the Fe centers by altering the crystal field of the Fe–N portion through the introduction of sacrificial bonds.[162] Selective breaking of the sacrificial Fe–S bond resulted in electron-withdrawing sulfur oxides in the Fe center. The reduced electron localization around the Fe center gave the catalyst excellent ORR activity and remarkable stability, which facilitated the desorption of ORR intermediates.

3.4. Stress-induced spin state change

Changes in catalyst geometry induce strain effects that affect the spin polarization of active centers and the changes of charge density. Zhang *et al.* succeeded in introducing strain effects on the active C–C bond near the edge graphite nitrogen, which increased the proper spin polarization and charge density of the carbon active center, and kinetically favoured the adsorption of O_2 and the activation of O-containing intermediates.[189] The spin-polarization strategy allows the construction of highly curved carbon-based multinuclear metal electrocatalysts with improved ORR performance by introducing strain effects. Dong *et al.* designed magical concave Pt–Zn nanocubes with high-index faceted platinum skins, which produced a strain effect different from that of the ordinary cubes.[190] The length of the Pt–Pt bond was significantly shortened, which reduced oxygen-containing intermediates' adsorption energy on the platinum surface. Jiang *et al.* proposed a spin-state transition strategy modulated by axial Fe–O–Ti ligands to enhance the ORR activity of Fe centers.[191] Theoretical calculations showed that the Fe–O–Ti ligand in FeN_3O–O–Ti induces a low to medium spin-state transition to optimize the adsorption of O_2 on the FeN_3O. The magnetic moment of Fe increased from 1.51 μ_B (FeN_3O) to 3.52 μ_B (FeN_3O–O–Ti). The low to moderate spin transition provides better E_g filling for Fe, which favors O_2 affinity. FeN_3O–O–Ti has suitable O_2 adsorption energy (1.84 eV) and ICOHP value (1.88 eV), meaning a moderate binding strength of O_2. It was therefore inferred that FeN_3O–O–Ti may have convincing ORR activity.

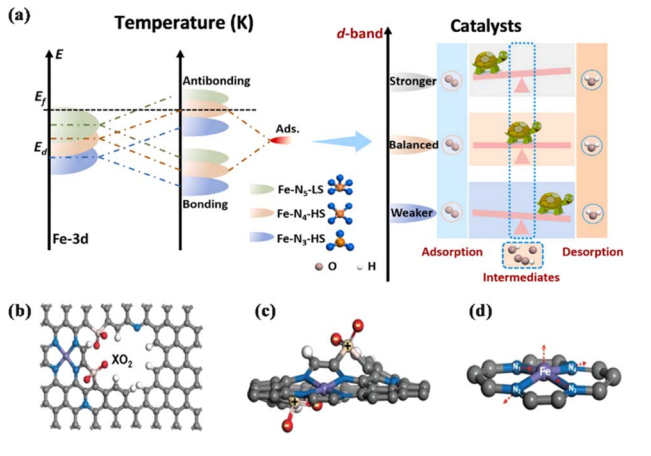

Fig. 22 (a) Schematic illustration of bond formation between the Fe–N–C and the adsorbates (left), and schematic illustration between the d-band centers and adsorption–desorption abilities of ORR intermediates (right). (b–d) Schematic diagrams of breaking FeN_4 square-planar coordination by introducing polar XO_2 (X = S, Se, and Te) groups. (a) Reproduced with permission.[188] Copyright 2022, Elsevier Ltd. (b–d) Reproduced with permission.[187] Copyright 2022, Wiley-VCH GmbH.

4. Challenges for optimizing atomic catalysts

4.1. Controlled synthesis

Accurate and controllable synthesis techniques play an important role in the fabrication of atomic catalysts. The active sites determine the catalytic activity and selectivity. Uniform active sites are conducive to the study of the relationship between structure and performance. At present, the common synthesis strategies for atomic catalysts include high temperature annealing and encapsulation.[13,66,192,193] Random dispersion is suitable for low metal loading, while high metal loading might lead to metal agglomeration since metal atoms migrate at high temperatures. The encapsulation strategy can satisfy the need to obtain DACs with definite structure, but the size of the selected precursor must match the carrier cage size. Using the steric hindrance of the carrier to inhibit atomic migration, Qu *et al.* constructed a diatomic catalyst with Fe_2, Cu_2 and Ir_2 sites by using the interface encapsulation strategy.[194] To prevent thermal migration during synthesis, the interface encapsulation carrier ZIF-8 with polydopamine was used, and the bimetallic precursor was anchored into the hollow nanocages (Fig. 23a–d). Bu *et al.* adopted a "pre-constrained metal twins" strategy to encapsulate an FeCo dimer into ZIF-8 *in situ* for the creation of adjacent Fe–N_4 and Co–N_4 geometric configurations (Fig. 23e).[180] Theoretical calculations showed that the interaction between Fe and Co optimizes the d-band center of the catalyst, optimizes the adsorption energy of oxygen intermediates, and improves the catalytic activity of the ORR/OER.

The major challenge of controlled synthesis is that the dynamic evolution of metal atoms and ligands during the synthesis is still not clear. To date, there have been some reports revealing this complex process. Huang *et al.* designed an atomization and sintering strategy to transfer Co nanoparticles

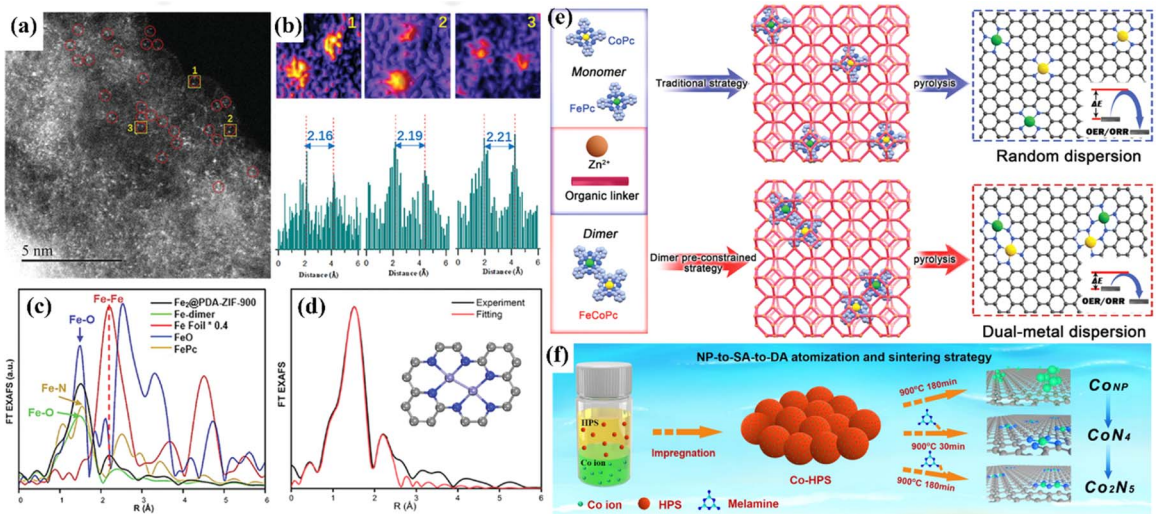

Fig. 23 (a) HAADF-STEM image. (b) Intensity profiles highlighted in yellow in (a). (c) Fe K edge FT EXAFS spectra. (d) FT EXAFS fitting spectrum at R space. (e) Schematic illustration of the traditional strategy and "pre-constrained metal twins" strategy for fabricating DACs. (f) Schematic diagram of the NP-to-SA-to-DA atomization and sintering strategy. (a–d) Reproduced with permission.[194] Copyright 2022, Wiley-VC. (e) Reproduced with permission.[180] Copyright 2022, Wiley-VC. (f) Reproduced with permission.[195] Copyright 2023, Nature.

to single-atom CoN_4 and then to diatomic Co_2N_5.[195] In this process, the nitrogen source played the role of stripping and fixing the metal atoms, and the Co_2N_5 sites were acquired by thermal migration spontaneous sintering (Fig. 23f). Wu *et al.* used *in situ* XAS to investigate the structural changes of the CoN_4 site during synthesis.[196] *In situ* XAS was used to monitor the conversion of inactive Co–OH/O to the active CoN_4 site. The conversion could not be completed below 700 °C, and the best activity was obtained at 900 °C. However, due to the limitation of advanced characterization techniques, it is still very difficult to dynamically study the whole process of the formation of active sites.

4.2. Increasing the density of active sites

For typical synthesis of SACs, it is usual to reduce the metal load on a high specific surface substrate to gain atomic dispersion and prevent aggregation, but due to the low metal load, there are few metal active sites. The number of catalytic active sites can be effectively increased by increasing the metal loading, but the probability of metal agglomeration increases gradually with the increase of metal loading. At present, the commonly used methods to increase metal loading and reduce agglomeration are to stabilize single metal atoms by introducing heteroatoms and using covalent coordination between the metal and nonmetal. Choi *et al.* loaded 5 wt% Pt in atomically dispersed form on a high sulfur doped zeolite template carbon by a wet impregnation method.[197] The rich sulfur doping and 3D carbon structure provided a stable loading environment.

Compared to SACs, the density of active sites in DACs and TACs can be enhanced. For instance, the loading capacity of iron in the monatomic iron catalyst (Fe–N_4–C) and the positive catalyst of diatomic iron (Fe_2–N_6–C-o) synthesized by Han *et al.* was 0.155 and 0.313 wt%, respectively.[181] More than 80% of the iron was identified as double metal sites by calculation, and the mean distance of Fe–Fe was 2.37 ± 0.31 Å. The Fe and Ni content in diatomic catalyst NiFe-DASC synthesized by Chen *et al.* using the pyrolysis strategy was 3.24 and 4.05 wt% respectively, which is twice the metal load of the Fe/Ni-SAC synthesized by the same method.[198] The HAADF-STEM images showed that the Ni and Fe atoms in the NiFe DASC are evenly dispersed, with a distance of about 0.24 nm between the Ni and Fe (Fig. 24a–g). Using the large number of periodic N–H functional groups in polymeric carbon nitride (PCN) as a metal coordination site, the metal can replace the H atom and can be fixed by N, avoiding agglomeration. Lu *et al.* used stepwise ion exchange and ligand removal strategies to synthesize low-coordination bimetallic atoms, where the content of Cu was up to 18.3 wt%.[199]

4.3. Enhancing intrinsic activity

To improve the inherent electrocatalytic activity of catalysts, the central metal atom and the coordination environment can be adjusted. Selecting an appropriate central metal atom as the active center can significantly improve the electrocatalytic activity and effectively adjust the product selectivity. For example, Fe-pyridine/pyrrole-N_4 and Mn-pyrrole-N_4 sites can catalyse the ORR, while the Co-pyrrole-N_4 site can catalyse the OER efficiently.[200] Cu is the only metal species that can convert CO_2 to C_{2+} in the CO_2RR.[201] The coordination environment includes a coordination atom, base atom and axial ligand. Unsaturated central metal atoms interact with ligands to regulate the metallic energy band, spin state, and charge redistribution to enhance the inherent activity. The heteroatoms on the base plane can regulate the electronic structure of the active site through long-range delocalization. In addition, the interaction of the active site with reactants and reaction intermediates during electrocatalysis can also effectively regulate its activity. Therefore, the inherent activity of the central metal atoms can

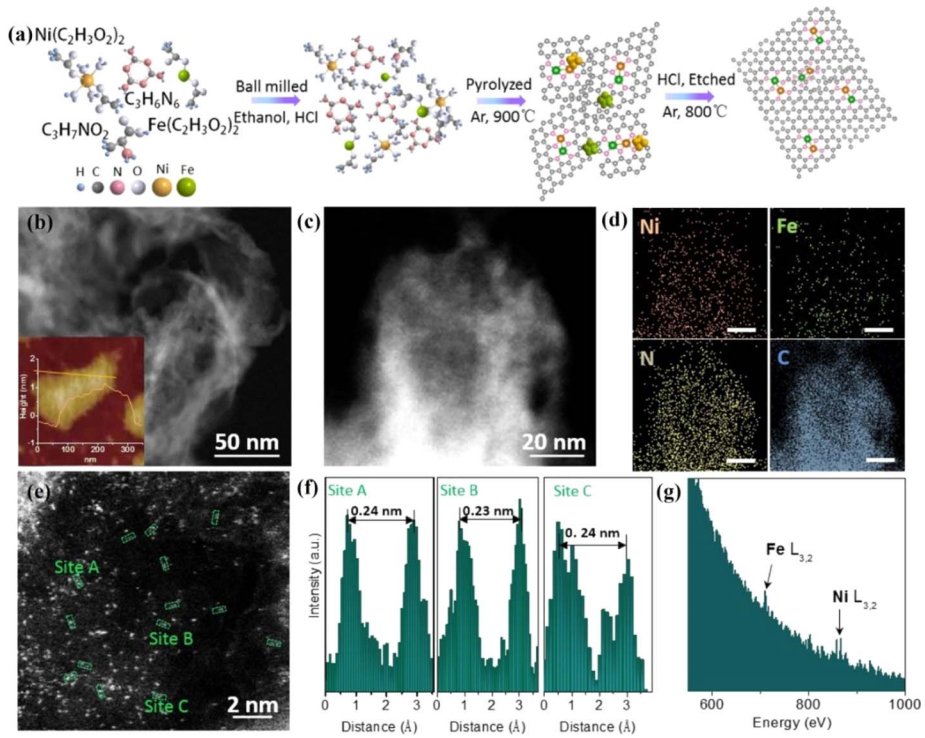

Fig. 24 (a) Schematic illustration of NiFe-DASC synthesis. (b) Dark-field scanning TEM and AFM (inset) images. (c) TEM image and (d) EDS elemental mapping of NiFe-DASC. (e) HAADF-STEM image of NiFe-DASC. (f) Intensity profiles of the three sites in (e). (g) Electronic energy loss spectroscopy (EELS) of NiFe-DASC. Reproduced with permission.[198] Copyright 2021, Nature.

be changed by adjusting the coordination environment. Zhang *et al.* synthesized a series of (Mn, Fe, Co, Ni, Cu or Zn) framework porphyrin (POF) materials, and found that the ORR activity of Co-POF was superior to that of Fe-POF.[202] Lu *et al.* constructed an Fe–N_2S_2 active site, and found that the activity of the CO_2RR was significantly optimized compared to that on an Fe–N_4 porphyrin.[203] On the Fe–N_4 porphyrin, the reduction to HCOOH is favourable at −0.70 V, while on the Fe–N_2S_2 porphyrin, CO_2 can be converted to HCOOH and CH_3OH at −0.38 V and −0.40 V, respectively (Fig. 25). The introduction of *para*-S atoms elongates the bond length of Fe–N, causing electrons to gather in the Fe–S bond, and the interaction between Fe and S is enhanced. Moreover, additional Fe orbitals in the Fe–N_2S_2 porphyrin can effectively regulate the adsorption/desorption energy of reaction intermediates and accelerate the CO_2RR.

In addition, adjacent active sites can regulate each other to promote the inherent electrocatalytic activity. Yu *et al.* demonstrated that the catalytic ORR activity was enhanced when the distance between the Fe–N_4 active sites was in the sub-nanometer level. When the distance between the two sites was less than 1.2 nm, the strong interaction between them altered the electronic structure and improved the inherent ORR activity. The activity is optimal when the distance is about 0.7 nm.[204] Qiao *et al.* demonstrated theoretically and experimentally that when the distance between Ni–N_4 and Cu–N_4 is

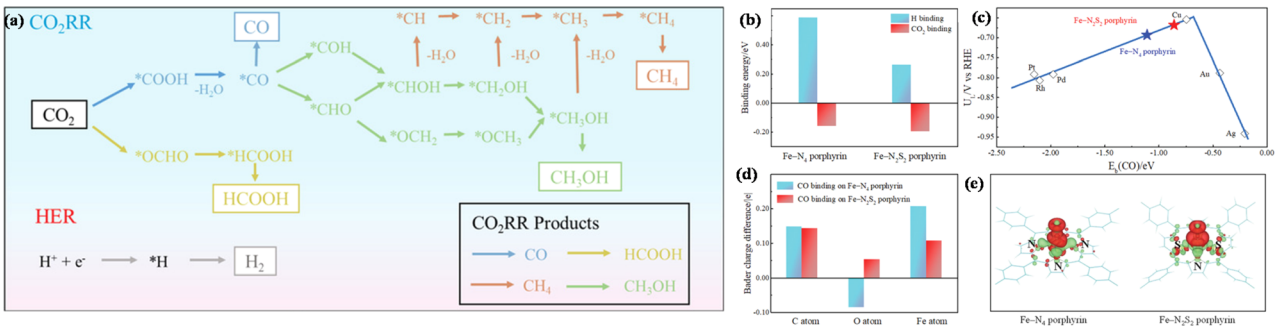

Fig. 25 (a) The schematic of elementary steps of the CO_2RR. (b) CO_2 and H binding energies. (c) Volcano plot. (d) Bader charge difference of C and O atoms of the CO molecule and Fe atom before and after CO binding. (e) Charge density difference of CO binding. Reproduced with permission.[203] Copyright 2021, Wiley-VCH GmbH.

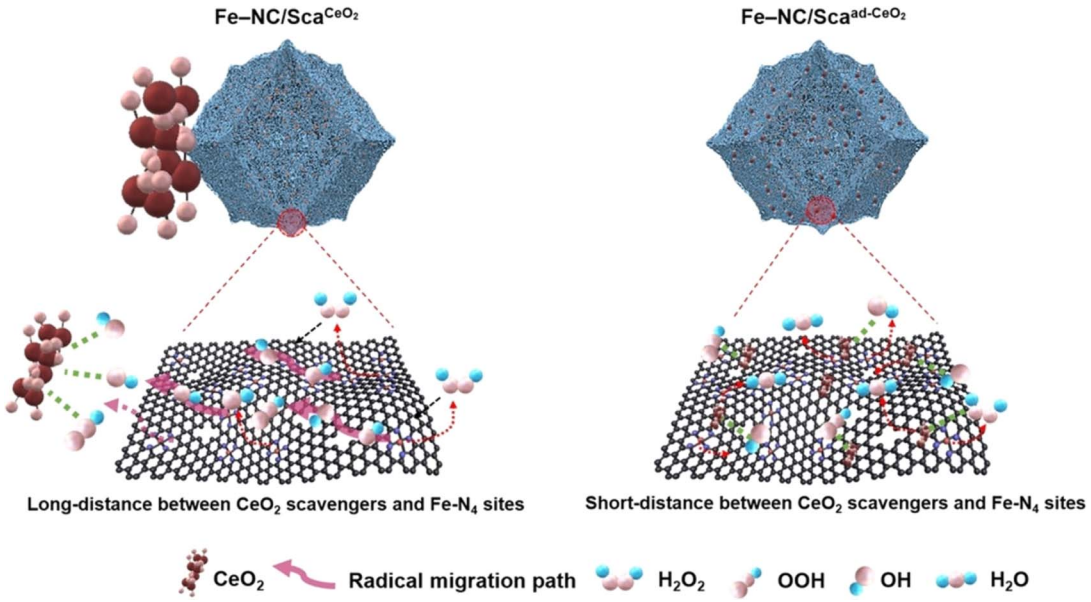

Fig. 26 Schematic illustration of the radical elimination behaviour. Reproduced with permission.[206] Copyright 2023, Wiley-VCH GmbH.

about 5.3 Å, the electronic structure of the active site can be effectively regulated to improve the selectivity and activity of the CO_2RR.[205]

4.4. Improving the stability

For atomic active sites, due to the high surface energy of metal atoms and the unsaturated coordination environment, the isolated metal sites will partially agglomerate under working conditions, resulting in a decrease in catalytic activity. The stability of active sites can be improved by enhancing the interaction between isolated metals and ligands and carriers. The electronegativity of the B atom is less than that of the N atom, which can effectively enhance the electron density of the Ni–N_4 center and strengthen the binding ability of the Ni site with reaction intermediates. Xin *et al.* synthesized a SAC (Ni–B/N–C) with Ni–B_1N_3 sites, which had a higher $E_{1/2}$ (0.87 V) than Ni–N–C (0.76 V) in the ORR, and was more stable than most Fe–N–C and Co–N–C catalysts.[174] In addition, based on the degradation mechanism of Fe–N–C SACs, some strategies have been proposed, such as the introduction of a co-catalyst and free radical scavenger in the active sites to effectively reduce the degradation. Sun *et al.* anchored CeO_2 NPs around Fe–N_4 active sites by an organic gas doping method. CeO_2 NPs were used to eliminate the $^{\cdot}OH$ and $HO_2^{\cdot}$ radical generated at the Fe–N_4 site (Fig. 26).[206] When the Fe-NC/Sca$^{ad\text{-}CeO_2}$ catalyst was assembled into a fuel cell, the attenuation of peak power density was reduced from 69% to 28%.

In addition, the active sites can be reconstructed under applied voltage, and the structure is restored upon removal of applied voltage, which is also considered to be a stable catalyst. Fontecave *et al.* reported nitrogen-doped graphene with CuN_4 sites (Cu–N–C), which reduced CO_2 to ethanol with an FE of 55%.[207] Under the applied voltage, the isolated CuN_4 transformed into copper clusters, and Cu–N–C recovered after the voltage was removed. Operando XAS showed that the transformed copper clusters were the active structure. During electrolysis, the reconstruction of CuN_4 in Cu–N–C was reversible.

5. Conclusions and outlook

In the past decade, SACs have made great progress in the field of electrocatalysis due to their unique geometry and electronic structures, which are expected to replace commercial precious metal-based catalysts. DACs with the interaction between metal dimers are also emerging and show excellent electrocatalytic activity, which can solve the limitation caused by SACs to a certain extent. To better suit multi-electron complex reactions, TACs have been developed, which provide more possibilities for the adsorption of intermediates, and are conducive to better study the relationship between the structure and electrocatalytic activity. In this review, we summarize the progress of SACs, DACs and TACs in electrocatalysis systematically. By using defect engineering and an atomic limiting strategy to design precursors, the number of central metal atoms and the coordination environment can be regulated for specific electrocatalytic reactions. Up to now, SACs and DACs designed by electronic regulation have made good progress in electrocatalysis. As a rising star, TACs are in the initial stage of development. In general, electrocatalysts with different nuclear numbers and uniform active sites have broad application prospects, but some problems still need to be solved.

(i) Controlled synthesis is still one of the biggest obstacles for atomic catalysts. At present, most of the atomic catalysts are synthesized by pyrolysis at high temperatures. The randomness of the coordination environment of the obtained catalysts is relatively large, and metal migration and agglomeration will inevitably occur. In addition, for DACs and TACs, active sites may possess multiple structures. By encapsulating precursors

into MOFs, COFs and other materials with pore structure, DACs and TACs can be synthesized through high-temperature pyrolysis. However, this method needs to ensure that the size of the precursor and the pores is compatible, which brings certain obstacles to the accurate control of the coordination environment. To solve the issue of migration and agglomeration of metal atoms during high temperature pyrolysis, Joule thermal synthesis technology with ultra-fast heating and cooling (millisecond level) processes has been developed. However, in the current synthesis technology, single-atom sites are unavoidably formed in DACs and TACs, resulting in the reduction of the target effective active sites. In addition, the atomic distance and configuration between active sites cannot be guaranteed to be consistent. The ratio of the target effective active sites to other structural sites plays a crucial role in determining catalytic activity. Therefore, it is pivotal to develop new and operable synthesis techniques to achieve precise regulation of the coordination environment and to better explain the relationship between structure and mechanism.

(ii) Atomic catalysts synthesized by controllable technology provide a good platform for studying the structure–activity relationships and reaction mechanisms. In catalytic processes, reaction intermediates adsorbed at active sites are dynamically evolved. In addition, the structures of some catalysts change under applied voltage, and therefore it is necessary to *in situ* detect the changes of active sites and reaction intermediates in catalytic reactions. At present, some *in situ* techniques have been developed, such as *in situ* XAS, IR, Raman, and TEM, but there are still issues in time accuracy and atomic resolution. For example, it is difficult to distinguish coordination atoms with similar atomic numbers and similar bonds (*e.g.* Co–N and Co–O). Therefore, advanced characterization techniques are needed to deeply understand the dynamic evolution of active sites during electrolysis.

(iii) At present, DFT calculations have been successfully applied to guide the selection of atomic catalysts. However, screening the coordination environment of metal center atoms is limited by computational cost and time, and traditional DFT calculations are not suitable for such a huge working system. With the development of computers, the first-principles high-throughput screening method will guide the experimental design of more excellent catalysts. In addition, the high-throughput method can also be used to screen the structures of reaction intermediates in catalytic reactions, and the combination with *in situ* characterizations will further promote the study of dynamic mechanisms. However, these calculations are carried out in an ideal environment, and the external conditions and internal environment in the electrocatalysis process are very complicated, which makes experimental results deviate from theoretical simulation to a certain extent, and a relatively large model is required to fully simulate the electrocatalytic environment. Therefore, new methods need to be developed in a timely manner.

(iv) Industrial grade catalysts need to have high activity and stability. Although atomic catalysts have made good progress, they are still in the basic research stage. At present, theoretical calculations of high-throughput screening can provide guidance for high-performance catalysts. Catalysts synthesized in the laboratory are in the gram scale, whereas the kilogram scale is commercially required. Therefore, catalyst amplification synthesis is also a key for commercial applications, since the mass-synthesized catalysts need to maintain high activity and stability. Moreover, the test of catalyst stability in the laboratory usually takes several hundred hours, but it falls far short of commercial requirements, since it'll take at least a few months. Therefore, more synthetic methods should be developed to synthesize catalysts that can effectively stabilize the active sites in corrosive electrolytes and reduce economic losses caused by frequent catalyst replacement.

In short, although atomic catalysts have made good progress in the field of electrocatalysis, there are still some issues to be addressed. However, we believe that with the development of new synthesis methods, characterization techniques and computing theories, atomic catalysts will play a significant role in the field of energy storage and conversion in the future.

Author contributions

All of the authors contributed to the literature search, writing and editing of this review.

Conflicts of interest

There are no conflicts to declare.

Acknowledgements

This work was supported by the National Natural Science Foundation of China (No. 22075099) and the Natural Science Foundation of Jilin Province (No. 20220101051JC).

Notes and references

1 A. Wang, J. Li and T. Zhang, *Nat. Rev. Chem*, 2018, **2**, 65–81.
2 L. Xu, P. Trogadas and M.-O. Coppens, *Adv. Energy Mater.*, 2023, **13**, 2302974.
3 L. Xiao, L. Qi, J. Sun, A. Husile, S. Zhang, Z. Wang and J. Guan, *Nano Energy*, 2024, **120**, 109155.
4 Y.-X. Zhao, J.-H. Wen, P. Li, P.-F. Zhang, S.-N. Wang, D.-C. Li, J.-M. Dou, Y.-W. Li, H.-Y. Ma and L. Xu, *Angew. Chem., Int. Ed.*, 2023, **62**, e202216950.
5 J. Chang, Q. Zhang, J. Yu, W. Jing, S. Wang, G. Yin, G. I. N. Waterhouse and S. Lu, *Adv. Sci.*, 2023, **10**, 2301656.
6 J. Quílez-Bermejo, S. García-Dalí, A. Daouli, A. Zitolo, R. L. S. Canevesi, M. Emo, M. T. Izquierdo, M. Badawi, A. Celzard and V. Fierro, *Adv. Funct. Mater.*, 2023, **33**, 2300405.
7 T. Sun, W. Zang, J. Sun, C. Li, J. Fan, E. Liu and J. Wang, *Adv. Funct. Mater.*, 2023, **33**, 2301526.
8 S. Chen, Y. Gao, W. Wang, O. V. Prezhdo and L. Xu, *ACS Nano*, 2023, **17**, 1522–1532.
9 Y. Gao, B. Liu and D. Wang, *Adv. Mater.*, 2023, **35**, 2209654.
10 F. Humblot, J. P. Candy, F. Le Peltier, B. Didillon and J. M. Basset, *J. Catal.*, 1998, **179**, 459–468.

11 J. Corker, F. Lefebvre, C. Lécuyer, V. Dufaud, F. Quignard, A. Choplin, J. Evans and J.-M. Basset, *Science*, 1996, **271**, 966–969.
12 B. Qiao, A. Wang, X. Yang, L. F. Allard, Z. Jiang, Y. Cui, J. Liu, J. Li and T. Zhang, *Nat. Chem.*, 2011, **3**, 634–641.
13 C. Zhu, S. Fu, Q. Shi, D. Du and Y. Lin, *Angew. Chem., Int. Ed.*, 2017, **56**, 13944–13960.
14 T. Tang, Z. Wang and J. Guan, *Adv. Funct. Mater.*, 2022, **32**, 2111504.
15 X. Bai, J. Han, X. Niu and J. Guan, *Nano Res.*, 2023, **16**, 10796–10802.
16 T. Tang, Z. Wang and J. Guan, *Coord. Chem. Rev.*, 2023, **492**, 215288.
17 L. Sun, V. Reddu and X. Wang, *Chem. Soc. Rev.*, 2022, **51**, 8923–8956.
18 B. Zhang, Y. Chen, J. Wang, H. Pan and W. Sun, *Adv. Funct. Mater.*, 2022, **32**, 2202227.
19 Y. Zhou, R. Lu, X. Tao, Z. Qiu, G. Chen, J. Yang, Y. Zhao, X. Feng and K. Müllen, *J. Am. Chem. Soc.*, 2023, **145**, 3647–3655.
20 Y. Chen, J. Mao, H. Zhou, L. Xing, S. Qiao, J. Yuan, B. Mei, Z. Wei, S. Zhao, Y. Tang and C. Liu, *Adv. Funct. Mater.*, 2023, 2311664.
21 W. Pei, S. Zhou, J. Zhao, X. Xu, Y. Du and S. X. Dou, *Nano Energy*, 2020, **76**, 105049.
22 Q.-F. Chen, Y. Xiao, R.-Z. Liao and M.-T. Zhang, *CCS Chem.*, 2022, **5**, 245–256.
23 D. E. Canfield, A. N. Glazer and P. G. Falkowski, *Science*, 2010, **330**, 192–196.
24 R. L. Robson, R. R. Eady, T. H. Richardson, R. W. Miller, M. Hawkins and J. R. Postgate, *Nature*, 1986, **322**, 388–390.
25 B. K. Burgess and D. J. Lowe, *Chem. Rev.*, 1996, **96**, 2983–3012.
26 J. Rittle and J. C. Peters, *J. Am. Chem. Soc.*, 2016, **138**, 4243–4248.
27 Z. Wei, J. He, Y. Yang, Z. Xia, Y. Feng and J. Ma, *J. Energy Chem.*, 2021, **53**, 303–308.
28 P. Saha, S. Amanullah and A. Dey, *J. Am. Chem. Soc.*, 2020, **142**, 17312–17317.
29 J. Deng, H. Li, J. Xiao, Y. Tu, D. Deng, H. Yang, H. Tian, J. Li, P. Ren and X. Bao, *Energy Environ. Sci.*, 2015, **8**, 1594–1601.
30 B. Wurster, D. Grumelli, D. Hötger, R. Gutzler and K. Kern, *J. Am. Chem. Soc.*, 2016, **138**, 3623–3626.
31 S. Ji, Y. Chen, Q. Fu, Y. Chen, J. Dong, W. Chen, Z. Li, Y. Wang, L. Gu, W. He, C. Chen, Q. Peng, Y. Huang, X. Duan, D. Wang, C. Draxl and Y. Li, *J. Am. Chem. Soc.*, 2017, **139**, 9795–9798.
32 Y. Pan, R. Lin, Y. Chen, S. Liu, W. Zhu, X. Cao, W. Chen, K. Wu, W.-C. Cheong, Y. Wang, L. Zheng, J. Luo, Y. Lin, Y. Liu, C. Liu, J. Li, Q. Lu, X. Chen, D. Wang, Q. Peng, C. Chen and Y. Li, *J. Am. Chem. Soc.*, 2018, **140**, 4218–4221.
33 W. Ren, X. Tan, W. Yang, C. Jia, S. Xu, K. Wang, S. C. Smith and C. Zhao, *Angew. Chem., Int. Ed.*, 2019, **58**, 6972–6976.
34 Y. Yang, L. Zhang, Z. Hu, Y. Zheng, C. Tang, P. Chen, R. Wang, K. Qiu, J. Mao, T. Ling and S.-Z. Qiao, *Angew. Chem., Int. Ed.*, 2020, **59**, 4525–4531.
35 Q.-F. Chen, Z.-Y. Cheng, R.-Z. Liao and M.-T. Zhang, *J. Am. Chem. Soc.*, 2021, **143**, 19761–19768.
36 M. Liu, H. Chun, T.-C. Yang, S. J. Hong, C.-M. Yang, B. Han and L. Y. S. Lee, *ACS Nano*, 2022, **16**, 10657–10666.
37 Y.-X. Zhang, S. Zhang, H. Huang, X. Liu, B. Li, Y. Lee, X. Wang, Y. Bai, M. Sun, Y. Wu, S. Gong, X. Liu, Z. Zhuang, T. Tan and Z. Niu, *J. Am. Chem. Soc.*, 2023, **145**, 4819–4827.
38 X. Yan, D. Liu, P. Guo, Y. He, X. Wang, Z. Li, H. Pan, D. Sun, F. Fang and R. Wu, *Adv. Mater.*, 2023, **35**, 2210975.
39 X. Xie, Z. Zhai, L. Peng, J. Zhang, L. Shang and T. Zhang, *Sci. Bull.*, 2023, **68**, 2862–2875.
40 Y. Chen, J. Lin, B. Jia, X. Wang, S. Jiang and T. Ma, *Adv. Mater.*, 2022, **34**, 2201796.
41 L. Li, K. Yuan and Y. Chen, *Acc. Mater. Res.*, 2022, **3**, 584–596.
42 Y. Zhang, L. Guo, L. Tao, Y. Lu and S. Wang, *Small Methods*, 2019, **3**, 1800406.
43 S. Yuan, J. Zhang, L. Hu, J. Li, S. Li, Y. Gao, Q. Zhang, L. Gu, W. Yang, X. Feng and B. Wang, *Angew. Chem., Int. Ed.*, 2021, **60**, 21685–21690.
44 R. Jiang, Z. Qiao, H. Xu and D. Cao, *Chin. J. Catal.*, 2023, **48**, 224–234.
45 L. Zhang, Y. Jia, G. Gao, X. Yan, N. Chen, J. Chen, M. T. Soo, B. Wood, D. Yang, A. Du and X. Yao, *Chem*, 2018, **4**, 285–297.
46 J. Liu, M. Jiao, B. Mei, Y. Tong, Y. Li, M. Ruan, P. Song, G. Sun, L. Jiang, Y. Wang, Z. Jiang, L. Gu, Z. Zhou and W. Xu, *Angew Chem. Int. Ed. Engl.*, 2019, **58**, 1163–1167.
47 J. Wan, W. Chen, C. Jia, L. Zheng, J. Dong, X. Zheng, Y. Wang, W. Yan, C. Chen, Q. Peng, D. Wang and Y. Li, *Adv. Mater.*, 2018, **30**, 1705369.
48 J. Jiao, R. Lin, S. Liu, W.-C. Cheong, C. Zhang, Z. Chen, Y. Pan, J. Tang, K. Wu, S.-F. Hung, H. M. Chen, L. Zheng, Q. Lu, X. Yang, B. Xu, H. Xiao, J. Li, D. Wang, Q. Peng, C. Chen and Y. Li, *Nat. Chem.*, 2019, **11**, 222–228.
49 L. Zhang, J. M. T. A. Fischer, Y. Jia, X. Yan, W. Xu, X. Wang, J. Chen, D. Yang, H. Liu, L. Zhuang, M. Hankel, D. J. Searles, K. Huang, S. Feng, C. L. Brown and X. Yao, *J. Am. Chem. Soc.*, 2018, **140**, 10757–10763.
50 J. Liang, Y. Jiao, M. Jaroniec and S. Z. Qiao, *Angew. Chem., Int. Ed.*, 2012, **51**, 11496–11500.
51 X. Bai, J. Han, S. Chen, X. Niu and J. Guan, *Chin. J. Catal.*, 2023, **54**, 212–219.
52 Z. Wang, C. Li, Y. Liu, Y. Wu, S. Zhang and C. Deng, *J. Energy Chem.*, 2023, **83**, 264–274.
53 L. Li, W. Yu, W. Gong, H. Wang, C.-L. Chiang, Y. Lin, J. Zhao, L. Zhang, J.-M. Lee and G. Zou, *Appl. Catal., B*, 2023, **321**, 122038.
54 J. Han and J. Guan, *Chin. J. Catal.*, 2023, **49**, 1–4.
55 Q. Sun, C. Jia, Y. Zhao and C. Zhao, *Chin. J. Catal.*, 2022, **43**, 1547–1597.
56 J. Li, L. Zhang, K. Doyle-Davis, R. Li and X. Sun, *Carbon Energy*, 2020, **2**, 488–520.
57 J. Han, X. Meng, L. Lu, J. Bian, Z. Li and C. Sun, *Adv. Funct. Mater.*, 2019, **29**, 1808872.

58 V. Hasija, S. Patial, P. Raizada, A. Aslam Parwaz Khan, A. M. Asiri, Q. Van Le, V.-H. Nguyen and P. Singh, *Coord. Chem. Rev.*, 2022, **452**, 214298.
59 N. Han, Y. Wang, L. Ma, J. Wen, J. Li, H. Zheng, K. Nie, X. Wang, F. Zhao, Y. Li, J. Fan, J. Zhong, T. Wu, D. J. Miller, J. Lu, S.-T. Lee and Y. Li, *Chem*, 2017, **3**, 652–664.
60 L. Xiao, Z. Wang and J. Guan, *Adv. Funct. Mater.*, 2023, 2310195.
61 Y. Chen, S. Ji, Y. Wang, J. Dong, W. Chen, Z. Li, R. Shen, L. Zheng, Z. Zhuang, D. Wang and Y. Li, *Angew. Chem., Int. Ed.*, 2017, **56**, 6937–6941.
62 W. Chen, J. Pei, C.-T. He, J. Wan, H. Ren, Y. Wang, J. Dong, K. Wu, W.-C. Cheong, J. Mao, X. Zheng, W. Yan, Z. Zhuang, C. Chen, Q. Peng, D. Wang and Y. Li, *Adv. Mater.*, 2018, **30**, 1800396.
63 Y. Yue, P. Cai, K. Xu, H. Li, H. Chen, H.-C. Zhou and N. Huang, *J. Am. Chem. Soc.*, 2021, **143**, 18052–18060.
64 C.-X. Zhao, J.-N. Liu, J. Wang, C. Wang, X. Guo, X.-Y. Li, X. Chen, L. Song, B.-Q. Li and Q. Zhang, *Sci. Adv.*, 2022, **8**, eabn5091.
65 W.-H. Li, J. Yang and D. Wang, *Angew. Chem., Int. Ed.*, 2022, **61**, e202213318.
66 R. Li and D. Wang, *Adv. Energy Mater.*, 2022, **12**, 2103564.
67 H. Zhang, X. Jin, J.-M. Lee and X. Wang, *ACS Nano*, 2022, **16**, 17572–17592.
68 P. Zhu, X. Xiong, D. Wang and Y. Li, *Adv. Energy Mater.*, 2023, **13**, 2300884.
69 L. Xiao, Z. Wang and J. Guan, *Chem. Sci.*, 2023, **14**, 12850–12868.
70 T. Tang, Z. Wang and J. Guan, *Chin. J. Catal.*, 2022, **43**, 636–678.
71 T. Tang, S. Li, J. Sun, Z. Wang and J. Guan, *Nano Res.*, 2022, **15**, 8714–8750.
72 Y. Yang, Y. Yu, J. Li, Q. Chen, Y. Du, P. Rao, R. Li, C. Jia, Z. Kang, P. Deng, Y. Shen and X. Tian, *Nano-Micro Lett.*, 2021, **13**, 160.
73 J. Park, S. Lee, H.-E. Kim, A. Cho, S. Kim, Y. Ye, J. W. Han, H. Lee, J. H. Jang and J. Lee, *Angew. Chem., Int. Ed.*, 2019, **58**, 16038–16042.
74 K. Jiang, B. Liu, M. Luo, S. Ning, M. Peng, Y. Zhao, Y.-R. Lu, T.-S. Chan, F. M. F. de Groot and Y. Tan, *Nat. Commun.*, 2019, **10**, 1743.
75 C. Tsounis, B. Subhash, P. V. Kumar, N. M. Bedford, Y. Zhao, J. Shenoy, Z. Ma, D. Zhang, C. Y. Toe, S. Cheong, R. D. Tilley, X. Lu, L. Dai, Z. Han and R. Amal, *Adv. Funct. Mater.*, 2022, **32**, 2203067.
76 W. Wang, Y. Wu, Y. Lin, J. Yao, X. Wu, C. Wu, X. Zuo, Q. Yang, B. Ge, L. Yang, G. Li, S. Chou, W. Li and Y. Jiang, *Adv. Funct. Mater.*, 2022, **32**, 2108464.
77 H. Yan, C. Tian, L. Wang, A. Wu, M. Meng, L. Zhao and H. Fu, *Angew. Chem., Int. Ed.*, 2015, **54**, 6325–6329.
78 Q. Jin, N. Liu, C. Dai, R. Xu, B. Wu, G. Yu, B. Chen and Y. Du, *Adv. Energy Mater.*, 2020, **10**, 2000291.
79 M. Li, J. Yu, Q. Liu, J. Liu, R. Chen, J. Zhu, R. Li and J. Wang, *ACS Sustain. Chem. Eng.*, 2022, **10**, 13505–13513.
80 J. Wang, X. Ge, L. Shao, J. Zhang, D. Peng, G. Zou, H. Hou, W. Deng, S. Xu, X. Ji and W. Zhang, *Mater. Today Energy*, 2020, **17**, 100436.
81 J. Yin, Q. Fan, Y. Li, F. Cheng, P. Zhou, P. Xi and S. Sun, *J. Am. Chem. Soc.*, 2016, **138**, 14546–14549.
82 J. Han and J. Guan, *Nano Res.*, 2023, **16**, 1913–1966.
83 S. Chen, T. Zhang, J. Han, H. Qi, S. Jiao, C. Hou and J. Guan, *Nano Res. Energy*, 2024, **3**, e9120106.
84 T. Tang, Z. Duan, D. Baimanov, X. Bai, X. Liu, L. Wang, Z. Wang and J. Guan, *Nano Res.*, 2023, **16**, 2218–2223.
85 H. Xu, T. Liu, S. Bai, L. Li, Y. Zhu, J. Wang, S. Yang, Y. Li, Q. Shao and X. Huang, *Nano Lett.*, 2020, **20**, 5482–5489.
86 Q. Wang, Z. Zhang, C. Cai, M. Wang, Z. L. Zhao, M. Li, X. Huang, S. Han, H. Zhou, Z. Feng, L. Li, J. Li, H. Xu, J. S. Francisco and M. Gu, *J. Am. Chem. Soc.*, 2021, **143**, 13605–13615.
87 X. Bai, Y. Wang, J. Han, X. Niu and J. Guan, *Appl. Catal., B*, 2023, **337**, 122966.
88 P. Kumar, K. Kannimuthu, A. S. Zeraati, S. Roy, X. Wang, X. Wang, S. Samanta, K. A. Miller, M. Molina, D. Trivedi, J. Abed, M. A. Campos Mata, H. Al-Mahayni, J. Baltrusaitis, G. Shimizu, Y. A. Wu, A. Seifitokaldani, E. H. Sargent, P. M. Ajayan, J. Hu and M. G. Kibria, *J. Am. Chem. Soc.*, 2023, **145**, 8052–8063.
89 Q. Shi, C. Zhu, D. Du and Y. Lin, *Chem. Soc. Rev.*, 2019, **48**, 3181–3192.
90 Y. Lee, J. Suntivich, K. J. May, E. E. Perry and Y. Shao-Horn, *J. Phys. Chem. Lett.*, 2012, **3**, 399–404.
91 W. T. Hong, M. Risch, K. A. Stoerzinger, A. Grimaud, J. Suntivich and Y. Shao-Horn, *Energy Environ. Sci.*, 2015, **8**, 1404–1427.
92 C. Zhang, Y.-C. Wang, B. An, R. Huang, C. Wang, Z. Zhou and W. Lin, *Adv. Mater.*, 2017, **29**, 1604556.
93 Q. Liu, X. Liu, L. Zheng and J. Shui, *Angew. Chem., Int. Ed.*, 2018, **57**, 1204–1208.
94 M. Luo, Z. Zhao, Y. Zhang, Y. Sun, Y. Xing, F. Lv, Y. Yang, X. Zhang, S. Hwang, Y. Qin, J.-Y. Ma, F. Lin, D. Su, G. Lu and S. Guo, *Nature*, 2019, **574**, 81–85.
95 X. Han, X. Ling, Y. Wang, T. Ma, C. Zhong, W. Hu and Y. Deng, *Angew. Chem., Int. Ed.*, 2019, **58**, 5359–5364.
96 C. Xia, Y. Xia, P. Zhu, L. Fan and H. Wang, *Science*, 2019, **366**, 226–231.
97 J. K. Nørskov, J. Rossmeisl, A. Logadottir, L. Lindqvist, J. R. Kitchin, T. Bligaard and H. Jónsson, *J. Phys. Chem. B*, 2004, **108**, 17886–17892.
98 C.-X. Zhao, B.-Q. Li, J.-N. Liu and Q. Zhang, *Angew. Chem., Int. Ed.*, 2021, **60**, 4448–4463.
99 X. Xie, L. Peng, H. Yang, G. I. N. Waterhouse, L. Shang and T. Zhang, *Adv. Mater.*, 2021, **33**, 2101038.
100 Y. Sun, L. Silvioli, N. R. Sahraie, W. Ju, J. Li, A. Zitolo, S. Li, A. Bagger, L. Arnarson, X. Wang, T. Moeller, D. Bernsmeier, J. Rossmeisl, F. Jaouen and P. Strasser, *J. Am. Chem. Soc.*, 2019, **141**, 12372–12381.
101 M. Kunitski, N. Eicke, P. Huber, J. Köhler, S. Zeller, J. Voigtsberger, N. Schlott, K. Henrichs, H. Sann, F. Trinter, L. P. H. Schmidt, A. Kalinin, M. S. Schöffler,

T. Jahnke, M. Lein and R. Dörner, *Nat. Commun.*, 2019, **10**, 1.
102 C. Wang, D. Wang, S. Liu, P. Jiang, Z. Lin, P. Xu, K. Yang, J. Lu, H. Tong, L. Hu, W. Zhang and Q. Chen, *J. Catal.*, 2020, **389**, 150–156.
103 J. Zhang, Y. Zhao, C. Chen, Y.-C. Huang, C.-L. Dong, C.-J. Chen, R.-S. Liu, C. Wang, K. Yan, Y. Li and G. Wang, *J. Am. Chem. Soc.*, 2019, **141**, 20118–20126.
104 Y. Wang, R. Shi, L. Shang, G. I. N. Waterhouse, J. Zhao, Q. Zhang, L. Gu and T. Zhang, *Angew. Chem., Int. Ed.*, 2020, **59**, 13057–13062.
105 Q. Zhao, Y. Wang, W.-H. Lai, F. Xiao, Y. Lyu, C. Liao and M. Shao, *Energy Environ. Sci.*, 2021, **14**, 5444–5456.
106 Y. Zhao, J. Liang, C. Wang, J. Ma and G. G. Wallace, *Adv. Energy Mater.*, 2018, **8**, 1702524.
107 X. Zu, X. Li, W. Liu, Y. Sun, J. Xu, T. Yao, W. Yan, S. Gao, C. Wang, S. Wei and Y. Xie, *Adv. Mater.*, 2019, **31**, 1808135.
108 Z. Jiang, T. Wang, J. Pei, H. Shang, D. Zhou, H. Li, J. Dong, Y. Wang, R. Cao, Z. Zhuang, W. Chen, D. Wang, J. Zhang and Y. Li, *Energy Environ. Sci.*, 2020, **13**, 2856–2863.
109 S. Kusama, T. Saito, H. Hashiba, A. Sakai and S. Yotsuhashi, *ACS Catal.*, 2017, **7**, 8382–8385.
110 K. Zhao, X. Nie, H. Wang, S. Chen, X. Quan, H. Yu, W. Choi, G. Zhang, B. Kim and J. G. Chen, *Nat. Commun.*, 2020, **11**, 2455.
111 T. Wang, L. Xu, Z. Chen, L. Guo, Y. Zhang, R. Li and T. Peng, *Appl. Catal., B*, 2021, **291**, 120128.
112 Z. Weng, Y. Wu, M. Wang, J. Jiang, K. Yang, S. Huo, X.-F. Wang, Q. Ma, G. W. Brudvig, V. S. Batista, Y. Liang, Z. Feng and H. Wang, *Nat. Commun.*, 2018, **9**, 415.
113 C. Zhang, S. Yang, J. Wu, M. Liu, S. Yazdi, M. Ren, J. Sha, J. Zhong, K. Nie, A. S. Jalilov, Z. Li, H. Li, B. I. Yakobson, Q. Wu, E. Ringe, H. Xu, P. M. Ajayan and J. M. Tour, *Adv. Energy Mater.*, 2018, **8**, 1703487.
114 T. Tang, Z. Wang and J. Guan, *Acta Phys.-Chim. Sin.*, 2022, **39**, 2208033.
115 Q. Chang, Y. Liu, J.-H. Lee, D. Ologunagba, S. Hwang, Z. Xie, S. Kattel, J. H. Lee and J. G. Chen, *J. Am. Chem. Soc.*, 2022, **144**, 16131–16138.
116 J. Wang, Y.-C. Huang, Y. Wang, H. Deng, Y. Shi, D. Wei, M. Li, C.-L. Dong, H. Jin, S. S. Mao and S. Shen, *ACS Catal.*, 2023, **13**, 2374–2385.
117 Z. Ma, T. Wan, D. Zhang, J. A. Yuwono, C. Tsounis, J. Jiang, Y.-H. Chou, X. Lu, P. V. Kumar, Y. H. Ng, D. Chu, C. Y. Toe, Z. Han and R. Amal, *ACS Nano*, 2023, **17**, 2387–2398.
118 H. Li, F. Pan, C. Qin, T. Wang and K.-J. Chen, *Adv. Energy Mater.*, 2023, **13**, 2301378.
119 M. Humayun, M. Israr, A. Khan and M. Bououdina, *Nano Energy*, 2023, **113**, 108570.
120 L. Han, X. Liu, J. Chen, R. Lin, H. Liu, F. Lü, S. Bak, Z. Liang, S. Zhao, E. Stavitski, J. Luo, R. R. Adzic and H. L. Xin, *Angew. Chem., Int. Ed.*, 2019, **58**, 2321–2325.
121 Z. Xue, X. Zhang, J. Qin and R. Liu, *J. Energy Chem.*, 2021, **57**, 443–450.
122 J. Han and J. Guan, *Chin. J. Catal.*, 2023, **47**, 1–31.
123 Y. Li, C. Chen, R. Cao, Z. Pan, H. He and K. Zhou, *Appl. Catal., B*, 2020, **268**, 118747.
124 N. Zhang, X. Zhang, Y. Kang, C. Ye, R. Jin, H. Yan, R. Lin, J. Yang, Q. Xu, Y. Wang, Q. Zhang, L. Gu, L. Liu, W. Song, J. Liu, D. Wang and Y. Li, *Angew. Chem., Int. Ed.*, 2021, **60**, 13388–13393.
125 X. Zhao, K. Zhao, Y. Liu, Y. Su, S. Chen, H. Yu and X. Quan, *ACS Catal.*, 2022, **12**, 11412–11420.
126 T. Tang, Y. Wang, J. Han, Q. Zhang, X. Bai, X. Niu, Z. Wang and J. Guan, *Chin. J. Catal.*, 2023, **46**, 48–55.
127 Y. Ying, X. Luo, J. Qiao and H. Huang, *Adv. Funct. Mater.*, 2021, **31**, 2007423.
128 Y. Yang, Y. Qian, H. Li, Z. Zhang, Y. Mu, D. Do, B. Zhou, J. Dong, W. Yan, Y. Qin, L. Fang, R. Feng, J. Zhou, P. Zhang, J. Dong, G. Yu, Y. Liu, X. Zhang and X. Fan, *Sci. Adv.*, 2020, **6**, eaba6586.
129 Y. Da, Z. Tian, R. Jiang, Y. Liu, X. Lian, S. Xi, Y. Shi, Y. Wang, H. Lu, B. Cui, J. Zhang, X. Han, W. Chen and W. Hu, *Sci. China Mater.*, 2023, **66**, 1389–1397.
130 M. Jiao, Z. Chen, N. Wang and L. Liu, *Appl. Catal., B*, 2023, **324**, 122244.
131 M. Jiang, F. Wang, F. Yang, H. He, J. Yang, W. Zhang, J. Luo, J. Zhang and C. Fu, *Nano Energy*, 2022, **93**, 106793.
132 L. Bai, C.-S. Hsu, D. T. L. Alexander, H. M. Chen and X. Hu, *J. Am. Chem. Soc.*, 2019, **141**, 14190–14199.
133 Z. Pei, X. F. Lu, H. Zhang, Y. Li, D. Luan and X. W. Lou, *Angew. Chem., Int. Ed.*, 2022, **61**, e202207537.
134 Y. He, X. Yang, Y. Li, L. Liu, S. Guo, C. Shu, F. Liu, Y. Liu, Q. Tan and G. Wu, *ACS Catal.*, 2022, **12**, 1216–1227.
135 J.-d. Yi, X. Gao, H. Zhou, W. Chen and Y. Wu, *Angew. Chem., Int. Ed.*, 2022, **61**, e202212329.
136 M. Feng, X. Wu, H. Cheng, Z. Fan, X. Li, F. Cui, S. Fan, Y. Dai, G. Lei and G. He, *J. Mater. Chem. A*, 2021, **9**, 23817–23827.
137 H. Cheng, X. Wu, M. Feng, X. Li, G. Lei, Z. Fan, D. Pan, F. Cui and G. He, *ACS Catal.*, 2021, **11**, 12673–12681.
138 S. Cao, S. Zhou, H. Chen, S. Wei, S. Liu, X. Lin, X. Chen, Z. Wang, W. Guo and X. Lu, *Energy Environ. Mater.*, 2021, **6**, e12287.
139 W. Yang, Z. Jia, B. Zhou, L. Chen, X. Ding, L. Jiao, H. Zheng, Z. Gao, Q. Wang and H. Li, *ACS Catal.*, 2023, **13**, 9695–9705.
140 D. Fang, P. Sun, S. Huang, Y. Shang, X. Li, D. Yan, Y. V. Lim, C.-Y. Su, B.-J. Su, J.-Y. Juang and H. Y. Yang, *ACS Mater. Lett.*, 2022, **4**, 1–10.
141 R. Wang, L.-Z. Dong, J.-W. Shi, M. Zhang, S.-L. Li, Y.-Q. Lan and J. Liu, *ACS Catal.*, 2024, **14**, 741–750.
142 D.-S. Huang, H.-L. Zhu, Z.-H. Zhao, J.-R. Huang, P.-Q. Liao and X.-M. Chen, *ACS Catal.*, 2022, **12**, 8444–8450.
143 M. Kato, M. Muto, N. Matsubara, Y. Uemura, Y. Wakisaka, T. Yoneuchi, D. Matsumura, T. Ishihara, T. Tokushima, S.-i. Noro, S. Takakusagi, K. Asakura and I. Yagi, *ACS Appl. Energy Mater.*, 2018, **1**, 2358–2364.
144 W. J. Li, Z. X. Lou, H. Y. Yuan, H. G. Yang and H. F. Wang, *J. Mater. Chem. A*, 2022, **10**, 16106–16114.
145 Z. W. Chen, L. X. Chen, M. Jiang, D. Chen, Z. L. Wang, X. Yao, C. V. Singh and Q. Jiang, *J. Mater. Chem. A*, 2020, **8**, 15086–15093.
146 X. Fu, X. Zhao, T.-B. Lu, M. Yuan and M. Wang, *Angew. Chem., Int. Ed.*, 2023, **62**, e202219242.

147 Y. Zhang, J. Yang, R. Ge, J. Zhang, J. M. Cairney, Y. Li, M. Zhu, S. Li and W. Li, *Coord. Chem. Rev.*, 2022, **461**, 214493.
148 G. Bae, S. Han, H.-S. Oh and C. H. Choi, *Angew. Chem., Int. Ed.*, 2023, **62**, e202219227.
149 Y. Wang, D. Wang and Y. Li, *Adv. Mater.*, 2021, **33**, 2008151.
150 P. Zhang, K. Chen, J. Li, M. Wang, M. Li, Y. Liu and Y. Pan, *Adv. Mater.*, 2023, **35**, 2303243.
151 Y. Zhu, J. Sokolowski, X. Song, Y. He, Y. Mei and G. Wu, *Adv. Energy Mater.*, 2020, **10**, 1902844.
152 D. Ji, L. Fan, L. Li, S. Peng, D. Yu, J. Song, S. Ramakrishna and S. Guo, *Adv. Mater.*, 2019, **31**, 1808267.
153 X. Li, W. Bi, M. Chen, Y. Sun, H. Ju, W. Yan, J. Zhu, X. Wu, W. Chu, C. Wu and Y. Xie, *J. Am. Chem. Soc.*, 2017, **139**, 14889–14892.
154 A. Guan, Z. Chen, Y. Quan, C. Peng, Z. Wang, T.-K. Sham, C. Yang, Y. Ji, L. Qian, X. Xu and G. Zheng, *ACS Energy Lett.*, 2020, **5**, 1044–1053.
155 M. Tong, F. Sun, G. Xing, C. Tian, L. Wang and H. Fu, *Angew. Chem., Int. Ed.*, 2023, **62**, e202314933.
156 H. Zhang, J. Li, S. Xi, Y. Du, X. Hai, J. Wang, H. Xu, G. Wu, J. Zhang, J. Lu and J. Wang, *Angew. Chem., Int. Ed.*, 2019, **58**, 14871–14876.
157 Y. Zhang, L. Jiao, W. Yang, C. Xie and H.-L. Jiang, *Angew. Chem., Int. Ed.*, 2021, **60**, 7607–7611.
158 W. Ren, X. Tan, W. Yang, C. Jia, S. Xu, K. Wang, S. C. Smith and C. Zhao, *Angew. Chem., Int. Ed.*, 2019, **58**, 6972–6976.
159 X.-M. Liang, H.-J. Wang, C. Zhang, D.-C. Zhong and T.-B. Lu, *Appl. Catal., B*, 2023, **322**, 122073.
160 Y.-N. Gong, C.-Y. Cao, W.-J. Shi, J.-H. Zhang, J.-H. Deng, T.-B. Lu and D.-C. Zhong, *Angew. Chem., Int. Ed.*, 2022, **61**, e202215187.
161 X. Yang, Y. Wang, G. Zhang, L. Du, L. Yang, M. Markiewicz, J.-y. Choi, R. Chenitz and S. Sun, *Appl. Catal., B*, 2020, **264**, 118523.
162 L. Yu, Y. Li and Y. Ruan, *Angew. Chem., Int. Ed.*, 2021, **60**, 25296–25301.
163 S. H. Lee, J. Kim, D. Y. Chung, J. M. Yoo, H. S. Lee, M. J. Kim, B. S. Mun, S. G. Kwon, Y.-E. Sung and T. Hyeon, *J. Am. Chem. Soc.*, 2019, **141**, 2035–2045.
164 B. Y. Xia, Y. Yan, N. Li, H. B. Wu, X. W. Lou and X. Wang, *Nat. Energy*, 2016, **1**, 15006.
165 M. Ferrandon, X. Wang, A. J. Kropf, D. J. Myers, G. Wu, C. M. Johnston and P. Zelenay, *Electrochim. Acta*, 2013, **110**, 282–291.
166 G. Yang, J. Zhu, P. Yuan, Y. Hu, G. Qu, B.-A. Lu, X. Xue, H. Yin, W. Cheng, J. Cheng, W. Xu, J. Li, J. Hu, S. Mu and J.-N. Zhang, *Nat. Commun.*, 2021, **12**, 1734.
167 S. Huang, Z. Qiao, P. Sun, K. Qiao, K. Pei, L. Yang, H. Xu, S. Wang, Y. Huang, Y. Yan and D. Cao, *Appl. Catal., B*, 2022, **317**, 121770.
168 J. Zhang, M. Zhang, Y. Zeng, J. Chen, L. Qiu, H. Zhou, C. Sun, Y. Yu, C. Zhu and Z. Zhu, *Small*, 2019, **15**, 1900307.
169 H. Shang, X. Zhou, J. Dong, A. Li, X. Zhao, Q. Liu, Y. Lin, J. Pei, Z. Li, Z. Jiang, D. Zhou, L. Zheng, Y. Wang, J. Zhou, Z. Yang, R. Cao, R. Sarangi, T. Sun, X. Yang, X. Zheng, W. Yan, Z. Zhuang, J. Li, W. Chen, D. Wang, J. Zhang and Y. Li, *Nat. Commun.*, 2020, **11**, 3049.
170 J. Wan, Z. Zhao, H. Shang, B. Peng, W. Chen, J. Pei, L. Zheng, J. Dong, R. Cao, R. Sarangi, Z. Jiang, D. Zhou, Z. Zhuang, J. Zhang, D. Wang and Y. Li, *J. Am. Chem. Soc.*, 2020, **142**, 8431–8439.
171 K. Li, S. Zhang, X. Zhang, S. Liu, H. Jiang, T. Jiang, C. Shen, Y. Yu and W. Chen, *Nano Lett.*, 2022, **22**, 1557–1565.
172 M. Huang, B. Deng, X. Zhao, Z. Zhang, F. Li, K. Li, Z. Cui, L. Kong, J. Lu, F. Dong, L. Zhang and P. Chen, *ACS Nano*, 2022, **16**, 2110–2119.
173 Z. Fan, R. Luo, Y. Zhang, B. Zhang, P. Zhai, Y. Zhang, C. Wang, J. Gao, W. Zhou, L. Sun and J. Hou, *Angew. Chem., Int. Ed.*, 2023, **62**, e202216326.
174 F. Wang, R. Zhang, Y. Zhang, Y. Li, J. Zhang, W. Yuan, H. Liu, F. Wang and H. L. Xin, *Adv. Funct. Mater.*, 2023, **33**, 2213863.
175 Y. Yang, K. Mao, S. Gao, H. Huang, G. Xia, Z. Lin, P. Jiang, C. Wang, H. Wang and Q. Chen, *Adv. Mater.*, 2018, **30**, 1801732.
176 T. Ding, X. Liu, Z. Tao, T. Liu, T. Chen, W. Zhang, X. Shen, D. Liu, S. Wang, B. Pang, D. Wu, L. Cao, L. Wang, T. Liu, Y. Li, H. Sheng, M. Zhu and T. Yao, *J. Am. Chem. Soc.*, 2021, **143**, 11317–11324.
177 X. Li, S. Mitchell, Y. Fang, J. Li, J. Perez-Ramirez and J. Lu, *Nat. Rev. Chem*, 2023, **7**, 754–767.
178 D.-C. Zhong, Y.-N. Gong, C. Zhang and T.-B. Lu, *Chem. Soc. Rev.*, 2023, **52**, 3170–3214.
179 Z. Pei, H. Zhang, Y. Guo, D. Luan, X. Gu and X. W. Lou, *Adv. Mater.*, 2023, 2306047.
180 M. Liu, N. Li, S. Cao, X. Wang, X. Lu, L. Kong, Y. Xu and X.-H. Bu, *Adv. Mater.*, 2022, **34**, 2107421.
181 Y. Wang, B. J. Park, V. K. Paidi, R. Huang, Y. Lee, K.-J. Noh, K.-S. Lee and J. W. Han, *ACS Energy Lett.*, 2022, **7**, 640–649.
182 X. Yi, H. Yang, X. Yang, X. Li, C. Yan, J. Zhang, L. Chen, J. Dong, J. Qin, G. Zhang, J. Wang, W. Li, Z. Zhou, G. Wu and X. Li, *Adv. Funct. Mater.*, 2023, 2309728.
183 B. Zhang, J. Hou, Y. Wu, S. Cao, Z. Li, X. Nie, Z. Gao and L. Sun, *Adv. Energy Mater.*, 2019, **9**, 1803693.
184 X. Yu, S. Lai, S. Xin, S. Chen, X. Zhang, X. She, T. Zhan, X. Zhao and D. Yang, *Appl. Catal., B*, 2021, **280**, 119437.
185 D. Chen, J. Zhu, X. Mu, R. Cheng, W. Li, S. Liu, Z. Pu, C. Lin and S. Mu, *Appl. Catal., B*, 2020, **268**, 118729.
186 L. Lv, R. Lu, J. Zhu, R. Yu, W. Zhang, E. Cui, X. Chen, Y. Dai, L. Cui, J. Li, L. Zhou, W. Chen, Z. Wang and L. Mai, *Angew. Chem., Int. Ed.*, 2023, **62**, e202303117.
187 R. Wang, L. Zhang, J. Shan, Y. Yang, J.-F. Lee, T.-Y. Chen, J. Mao, Y. Zhao, L. Yang, Z. Hu and T. Ling, *Adv. Sci.*, 2022, **9**, 2203917.
188 D. Xue, P. Yuan, S. Jiang, Y. Wei, Y. Zhou, C.-L. Dong, W. Yan, S. Mu and J.-N. Zhang, *Nano Energy*, 2023, **105**, 108020.
189 Y. Wang, W. Cheng, P. Yuan, G. Yang, S. Mu, J. Liang, H. Xia, K. Guo, M. Liu, S. Zhao, G. Qu, B.-A. Lu, Y. Hu, J. Hu and J.-N. Zhang, *Adv. Sci.*, 2021, **8**, 2102915.

190 M. Liu, B.-A. Lu, G. Yang, P. Yuan, H. Xia, Y. Wang, K. Guo, S. Zhao, J. Liu, Y. Yu, W. Yan, C.-L. Dong, J.-N. Zhang and S. Mu, *Adv. Sci.*, 2022, **9**, 2200147.

191 Y. Liu, X. Liu, Z. Lv, R. Liu, L. Li, J. Wang, W. Yang, X. Jiang, X. Feng and B. Wang, *Angew. Chem., Int. Ed.*, 2022, **61**, e202117617.

192 K. Maiti, S. Maiti, M. T. Curnan, H. J. Kim and J. W. Han, *Adv. Energy Mater.*, 2021, **11**, 2101670.

193 A. Pedersen, J. Barrio, A. Li, R. Jervis, D. J. L. Brett, M. M. Titirici and I. E. L. Stephens, *Adv. Energy Mater.*, 2022, **12**, 2102715.

194 K. Leng, J. Zhang, Y. Wang, D. Li, L. Bai, J. Shi, X. Li, L. Zheng, J. Bai and Y. Qu, *Adv. Funct. Mater.*, 2022, **32**, 2205637.

195 X. Wang, L. Xu, C. Li, C. Zhang, H. Yao, R. Xu, P. Cui, X. Zheng, M. Gu, J. Lee, H. Jiang and M. Huang, *Nat. Commun.*, 2023, **14**, 7210.

196 Y. He, Q. Shi, W. Shan, X. Li, A. J. Kropf, E. C. Wegener, J. Wright, S. Karakalos, D. Su, D. A. Cullen, G. Wang, D. J. Myers and G. Wu, *Angew. Chem., Int. Ed.*, 2021, **60**, 9516–9526.

197 C. H. Choi, M. Kim, H. C. Kwon, S. J. Cho, S. Yun, H.-T. Kim, K. J. J. Mayrhofer, H. Kim and M. Choi, *Nat. Commun.*, 2016, **7**, 10922.

198 Z. Zeng, L. Y. Gan, H. Bin Yang, X. Su, J. Gao, W. Liu, H. Matsumoto, J. Gong, J. Zhang, W. Cai, Z. Zhang, Y. Yan, B. Liu and P. Chen, *Nat. Commun.*, 2021, **12**, 4088.

199 X. Hai, Y. Zheng, Q. Yu, N. Guo, S. Xi, X. Zhao, S. Mitchell, X. Luo, V. Tulus, M. Wang, X. Sheng, L. Ren, X. Long, J. Li, P. He, H. Lin, Y. Cui, X. Peng, J. Shi, J. Wu, C. Zhang, R. Zou, G. Guillén-Gosálbez, J. Pérez-Ramírez, M. J. Koh, Y. Zhu, J. Li and J. Lu, *Nature*, 2023, **622**, 754–760.

200 H. Xu, D. Cheng, D. Cao and X. C. Zeng, *Nat. Catal.*, 2018, **1**, 339–348.

201 S. H. Lee, J. C. Lin, M. Farmand, A. T. Landers, J. T. Feaster, J. E. Avilés Acosta, J. W. Beeman, Y. Ye, J. Yano, A. Mehta, R. C. Davis, T. F. Jaramillo, C. Hahn and W. S. Drisdell, *J. Am. Chem. Soc.*, 2021, **143**, 588–592.

202 C.-X. Zhao, B.-Q. Li, J.-N. Liu, J.-Q. Huang and Q. Zhang, *Chin. Chem. Lett.*, 2019, **30**, 911–914.

203 S. Cao, S. Wei, X. Wei, S. Zhou, H. Chen, Y. Hu, Z. Wang, S. Liu, W. Guo and X. Lu, *Small*, 2021, **17**, 2100949.

204 Z. Jin, P. Li, Y. Meng, Z. Fang, D. Xiao and G. Yu, *Nat. Catal.*, 2021, **4**, 615–622.

205 D. Yao, C. Tang, X. Zhi, B. Johannessen, A. Slattery, S. Chern and S.-Z. Qiao, *Adv. Mater.*, 2022, **35**, 2209386.

206 X. Cheng, X. Jiang, S. Yin, L. Ji, Y. Yan, G. Li, R. Huang, C. Wang, H. Liao, Y. Jiang and S. Sun, *Angew. Chem., Int. Ed.*, 2023, **62**, e202306166.

207 D. Karapinar, N. T. Huan, N. Ranjbar Sahraie, J. Li, D. Wakerley, N. Touati, S. Zanna, D. Taverna, L. H. Galvão Tizei, A. Zitolo, F. Jaouen, V. Mougel and M. Fontecave, *Angew. Chem., Int. Ed.*, 2019, **58**, 15098–15103.